M 2018

U.PORTO
FEUP FACULDADE DE ENGENHARIA
UNIVERSIDADE DO PORTO

PASSIVE CONTROL ON TRANSONIC FLOW

STUDY OF CAVITY EFFECT ON NACA 4412 AIRFOIL

DIEGO CARLOS RUA MOREIRA

MASTER'S DISSERTATION PRESENTED TO
THE FACULTY OF ENGINEERING OF UNIVERSITY OF PORTO IN
COMPUTATIONAL MECHANICS

FACULDADE DE ENGENHARIA DA UNIVERSIDADE DO PORTO

Passive Control on Transonic Flow: Study of Cavity Effect on NACA 4412 Airfoil

Diego Carlos Rua Moreira

Dissertation Submitted for
Master's Degree in Computational Mechanics

Supervisors:
Dr. José Manuel de Almeida César de Sá – FEUP
Dr. Oluwa**mayo**kun B. Adetoro – Brunel University London
Dr. Rui Cardoso – Brunel University London

September 2018

Resumo

O presente trabalho traz as análises e resultados referentes a simulações realizadas em perfis modificados do aerofólio NACA 4412. O principal foco desta dissertação foi testar, com o auxílio de ferramentas CFD, novas configurações que pudessem gerar uma diminuição no arrasto ou melhorias aerodinâmicas gerais, se comparadas com a geometria original do aerofólio em questão.

As modificações feitas no perfil consistiram na inserção de uma cavidade redesenhada em duas localizações diferentes, e foram baseadas nos programas científicos EUROSHOCK, em um típico caso de controle passivo aplicado a escoamentos transônicos. O estudo estendeu conceitos já presentes na literatura e tentou avaliar quais comprimentos das cavidades trariam os melhores resultados.

De maneira a alcançar os objetivos estabelecidos, o presente trabalho abordou algumas etapas do projeto e discutiu muitos pontos relevantes, passando pela realização de uma revisão teórica, incluindo um resumo do modelo de turbulência usado, e pela metodologia empregada nas simulações, onde foram apresentados diversos aspectos da implementação, como geometrias, o processo de determinação da malha final e as condições de fronteiras empregadas.

Finalmente, os resultados foram apresentados, incluindo um teste de validação com dados experimentais presentes na literatura, simulações da geometria padrão do aerofólio que serviriam de base para os próximos testes e a discussão dos casos modificados, escopo principal do presente trabalho. Comparações entre os casos em relação aos coeficientes de sustentação e arrasto permitiram determinar qual configuração trouxe mais benefícios ao escoamento principal, potencialmente levando a uma economia de combustível e outras otimizações aerodinâmicas.

Palavras-chave – Controle de escoamento, Controle passivo de escoamento, Cavidade, Escoamento transônico, NACA 4412, CFD.

Abstract

The present work brings the results and analyses of simulations considering modified profiles of NACA 4412 airfoil. The main focus of this dissertation was to test new configurations using CFD that could generate drag reduction or overall aerodynamic improvements, if compared to the standard geometry of the referred airfoil.

The modifications made in the profile consisted of a redesigned cavity geometry in two different locations and were based in the EUROSHOCK programmes, in a typical case of passive control on a transonic flow. The study extended concepts already present in the literature and tried to assess optimal lengths of the cavities that could generate the best results.

In order to achieve its goals, the present work explored many levels of the project and discussed several other relevant points, passing through a theoretical review, with a summary of the turbulence model used, and the simulations methodology, where the main aspects of the implementation were discussed, like the geometries, the mesh determination process and the boundaries conditions applied.

Finally, the results were presented, including a validation test with experimental data from the literature, standard airfoil simulations to serve as baseline and the modified cases, main subject of the present work. Comparisons between the cases in terms of lift and drag coefficients allowed determining which configuration brought more benefits to the main flow, potentially leading to fuel saving and other aerodynamic optimizations.

Keywords – Flow control, Passive flow control, Cavity, Transonic flow, NACA 4412, CFD.

Acknowledgments

This dissertation is the result of many efforts, not only mine, but from people who I met along the way that made this project possible, and from others that were always there for me, passing through all the challenges together and cheering all my achievements.

I would like to start by thanking my supervisor from the Faculty of Engineering of University of Porto, **Dr. José César de Sá**, who gracefully was able to accommodate my ideas and interests, fulfilling what I was expecting from this master course and its final work.

I would like to express my sincere gratitude to my other supervisors, **Dr. Rui Cardoso** and **Dr. Mayo Adetoro**, who welcomed me in Brunel University London, and made my second stay in Uxbridge an enriching experience in many ways, personally and academically.

I would like to thank the **European Commission** for the opportunity of being part of the Erasmus+ 2017 Credit Mobility (2017-1-PT01-KA103-035245), whose funding was essential to make this happen.

Finally, I would like to give a special thanks to **all my family**, whose love and support echoed from thousand miles away, providing me the strength to continue pursuing my dreams. *Saudade* wouldn't even begin to describe…

For those who were there with me in this journey, **my friends and colleagues**, thank you.

Diego Carlos Rua Moreira

Brunel University London

Co-funded by the Erasmus+ Programme of the European Union

Contents

List of Figures

List of Tables

Acronyms and Symbols

AoA	Angle of Attack
CFD	Computational Fluid Dynamics
DERA	Defence Evaluation and Research Agency
DLR	*Deutsches Zentrum Für Luft- Und Raumfahrt*
DNS	Direct Numerical Simulation
HLFC	Hybrid Laminar Flow Control
LES	Large-Eddy Simulation
LES-NWM	Large-Eddy Simulation Near-Wall Modelling
LES-NWR	Large-Eddy Simulation Near-Wall Resolution
MTOW	Maximum Take-Off Weight
NACA	National Advisory Committee for Aeronautics
ONERA	*Office National d'Etudes Et De Recherches Aérospatiales*
RANS	Reynolds Averaged Navier-Stokes Simulations
VLES	Very Large-Eddy Simulation

a	Speed of sound
a_∞	Freestream speed of sound
c	Airfoil chord
C_d	Drag coefficient
C_L	Lift coefficient
$C_{P_{lower}}$	Pressure coefficient of the lower airfoil surface
$C_{P_{upper}}$	Pressure coefficient of the upper airfoil surface
C_p	Heat capacity at constant pressure
d	Distance from the field point to the nearest wall
g	Gravity acceleration
h_t	Stagnation enthalpy
L	Lift force

m	Maximum airfoil camber
M	Mach number
M_∞	Freestream Mach number
p	Maximum airfoil camber position
P	Pressure
P_∞	Freestream pressure
P_0	Ground level pressure
R	Specific ideal gas constant
Re	Reynolds number
s	Entropy
S	Sutherland constant
t	Maximum airfoil thickness
T	Fluid temperature
T_∞	Freestream temperature
T_0	Reference temperature
T_t	Stagnation temperature
U	Flow velocity
U_∞	Freestream velocity
$\vec{U}$	Velocity vector
$\vec{x}$	Spatial vector
y^+	Dimensionless wall distance
α	Angle of attack
γ	Adiabatic index or ratio of specific heats
δ	Displacement along y
ϵ	Dissipation of turbulence energy rate
κ	Turbulence kinetic energy
μ	Dynamic viscosity of the fluid
μ_0	Reference viscosity
ν	Kinematic viscosity of the fluid
ν_t	Eddy viscosity
ρ	Fluid density
$\sigma\left(\frac{x}{C}\right)$	Dimensionless camber function
τ	Stress tensor
$\tau\left(\frac{x}{C}\right)$	Dimensionless thickness function
ϕ	Potential velocity
ω	Specific dissipation of turbulence energy rate
Ω	Vorticity magnitude

Chapter 1

Introduction

1.1 - Context

The aerospace industry is constantly searching for new and optimized ways of making missions more cost-effective, comfortable and secure. Mankind has conquered the skies, but many problems arose with the inherently large-scale business associated with flying, especially in commercial aviation. The number of flights has reached a point of saturation in the globalized world [1], with overall costs, environmental impact and the business model itself representing a huge concern.

In the beginning, the main goal of the airlines was to provide an enjoyable and secure flight for an exclusive clientele, which was comfortable paying a premium to fly and travel in a more fast and efficient way. Cost were never a problem or, at least, not a priority at the moment [2].

However, as flying was becoming the main way of travel with the introduction of jets in the late 1950's [3], the industry through engineering research was more and more interested in reducing costs associated with its operation. Many steps can be taken to reduce an airliner operation cost and many companies have reached a limit where the relation between customer satisfaction and price cannot be downsized any longer [4].

In this context, fuel costs represented around 20% of the total costs of operation of the airlines in the year of 2016 [5], which can be improved by new technologies and enhanced aircrafts developed by the manufacturers. Moreover, reducing the fuel consumption helps the environment as well by limiting the carbon footprint of a mission, in a society that is increasingly moving towards renewable power sources and reducing fossil-based fuel usage.

An example of a recently developed aircraft with state-of-the-art technology related to fuel-saving, acoustic comfort and passenger well-being is the Boing's 787-10, also known as "Dreamliner", which can be seen in Figure 1.1.

Figure 1.1 – Boeing's 787-10, recent addition to the "Dreamliner" family [6].

The Boeing's 787-10 is a natural evolution of the 787-9 and the most recent addition to the "Dreamliner" family, which brought many features in terms of fuel-saving technologies. Some of these features are the use of composite materials, which reduces the weight and provides great strength to the aircraft structures; new developed bleedless[1] engines, with all-electrical systems, and the hybrid laminar flow control (HLFC) devices, first introduced on 787-9 and a type of passive flow control that aims to keep the flow in a laminar state as long as possible over the wing, with the introduction of tiny holes on the structure. This last one is especially aligned with the main purpose of the present work and is promised to reduce the drag significantly according to the manufacturer, consequently optimizing fuel consumption [7].

Although civil aviation has been the greater supporter for the recent advancements on fuel-saving technologies, both military and aerospace fields have proven to be great beneficiaries of such improvements as well. New materials, enhanced airfoil profiles and many other features help extreme nature missions to be more efficient, even when the cost is not the main concern. These features combined could lead to other improvements, such as new systems not implemented in the past due to weight limitations, less allocated space for fuel, greater maximum take-off weight (MTOW), among others.

1.2 - Flow Control Applied to Airfoils: An Overview

The Boeing's 787 aircraft family is just one example of how the research on new and enhanced aerospace systems and structures can be implemented on a more practical level,

[1] Bleedless Aircraft Engine or No-Bleed system is a technology that uses all the air of the engine internal flow to generate thrust and electrical power via generators. In a classic arrangement, part of the internal flow is used to pressurize the pneumatic system of the aircraft, known as pneumatic bleed. In the 787-10, the new developed bleedless engines have proven to save 1-2% of fuel at normal cruise conditions [8].

while many other companies have been testing new features on their products to adapt to an increasingly competitive market.

A lot of progress has been made throughout the past decades regarding ways of optimizing aerospace missions, and flow control, main focus of the present work, plays a major role on that matter. Many experiments on the subject have been performed testing a variety of features, from cavities and bumps to more complex structures such as modified flaps and flexible trailing edges [9], all of which changing or limiting the nature of the original flow.

The control of flow can be divided into two main classification groups, active and passive. As the name suggests, active flow control happens when there is energy consumption, and passive flow control occurs without or with minimal energy consumption. Both types of control represent a trade-off between cost, weight, operation and maintenance of such device and the real advantage to the mission. For example, an active device that reduces drastically the drag but consumes a lot of energy brings no real contribution to the mission compared to the actual configuration, and a passive modification could yield great results, but be really expensive to manufacture. Such balance is difficult to achieve, which justifies the amount of research on the subject with low practical outcome.

Many institutions and companies have spent a lot of resources searching for good and viable solutions during the past few decades. That is the case of the programmes EUROSHOCK I and II supported by the European Union. These programmes were a consortium between European space agencies such as DLR (*Deutsches Zentrum für Luft- und Raumfahrt*, German Aerospace Centre), ONERA (*Office National d'Etudes et de Recherches Aérospatiales*, French National Aerospace Research Centre) and DERA (Defence Evaluation and Research Agency, part of the UK Ministry of Defence, now dissolved), among other collaborators [10,11].

Totally inserted in the scope of the present work, the EUROSHOCK programmes made an extensive and comprehensive research on the effects of shock on the boundary layer of transonic flows around airfoils and how to avoid or minimize the problems caused by it in terms of drag reduction and flow separation.

In this context, several flow control devices were tested, and many other hypotheses assessed. In Figure 1.2, it is possible to observe a passive case with a cavity implementation, and, in Figure 1.3, some of the active flow control devices used as part of the EUROSHOCK programmes.

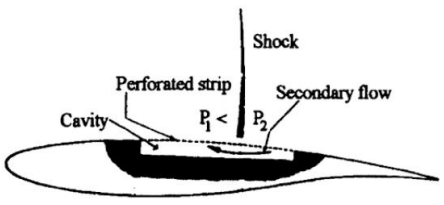

Figure 1.2 – Passive flow control device tested in the EUROSHOCK programmes [10].

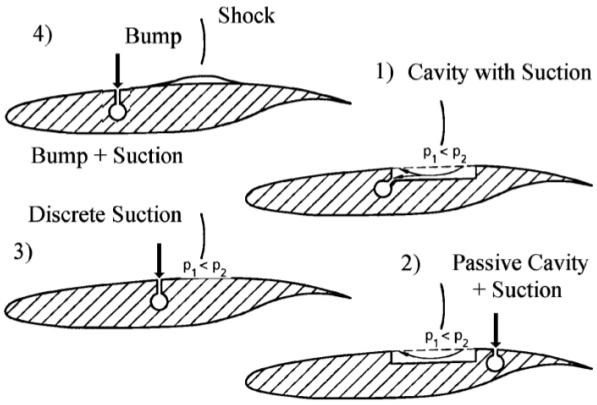

Figure 1.3 – Active flow control devices tested in the EUROSHOCK programmes [12].

The Figure 1.2 shows a passive flow control cavity, where it is represented the pressure differences and the recirculation, while Figure 1.3 presents four types of active devices for transonic flow control. Three of them involve suction combined with a geometric feature – cavity or bump – and one (represented in number 3) uses only the suction as control.

It was shown in the context of the EUROSHOCK programmes that the cavity by itself, even when covered by a perforated surface, produced an increase in total drag, although the wave-induced drag was reduced and the shock control and stabilization could be a feature to be explored in certain conditions [9]. These conclusions were limited to the airfoils tested and to a fixed geometry, which formed the main motivation of this work, presented in section 1.3.

1.3 - Motivation and Objectives

When the pressure distribution of a transonic flow over an airfoil is analysed, it is possible to see right away that two regions are formed due to the shock: a high and a low-pressure region. This state summed with the cavity configuration makes a passive suction possible – a secondary flow that forms in the opposite direction of the main flow, creating a recirculating type of flow (Figure 1.2).

All the tests involving the cavity configuration in the EUROSHOCK programmes were made with a fully developed cavity, some covered by perforated surfaces (Figure 1.2), some combined with suction devices (Figure 1.3). However, the secondary flow plays a major role in this type of flow control, with the passive suction effect created downstream and a possible reattachment of the flow yielding a drag reduction eventually. This represented the motivation and the starting point of the present work.

It is known that the cavity configuration explored in the EUROSHOCK programmes rises the total drag, even with the secondary flow recirculation [9]. However, the mass flow rate involved on that flow was fixed and limited by the cavity geometry. Therefore, it would be

just a matter of finding an ideal mass flow rate of that secondary flow that would produce the wanted drag reduction, with this mass flow rate defined by the area (or in 2D, length) of the upstream and the downstream "semi-cavity", both linked inside.

Thus, the main objective of the present work was to find this ideal area (or length) and expand the cavity configuration hypotheses proposed in the EUROSHOCK programmes by incrementing these lengths towards the original case, the fully developed cavity.

In summary, the objectives of the present work were:

- Implement a validation test of a transonic flow around a general airfoil profile (NACA 4412) and compare with the literature;
- Implement several cases with different angles of attack and observe flow separation in the same airfoil;
- Implement several cavity cases with different lengths in the same airfoil for a chosen angle of attack and assess lift and drag coefficients;
- Observe which cavity case produced drag reduction or flow reattachment (if produced) and make a final analysis.

1.4 - Conclusion and Dissertation Structure

In this chapter, a brief introduction was presented, covering the context, an overview on flow control and the main motivation and objectives of the present work.

The high operational costs of the aviation industry play an important role as supporting a lot of researches, although military and aerospace applications cannot be ignored. Flow control techniques and devices contribute on the matter by reducing drag and consequently saving fuel, or by just making the missions more efficient.

As a main motivation, a starting point was expanding the EUROSHOCK programmes conclusions regarding the use of a cavity as a passive flow control device. Successful implementations of the airfoil profile NACA 4412 with or without the cavity configuration represents the objectives of the current work, with the main goal being a drag reduction observation.

In this context, the next chapters will discuss the main aspects used in the present work in order to reach its goals:

- Chapter 2 makes a brief theoretical review regarding the analytical formulation of flows around airfoils and a quick introduction on turbulence models, especially the one used in the CFD simulations;
- Chapter 3 brings the project methodology, covering the outline, geometry, mesh attempts and final grid and main boundary conditions;
- Chapter 4 presents the results for all implementations made in the present work, together with case comparisons and lift and drag coefficients assessment;

- Chapter 5 concludes the dissertation, bringing the main remarks and relevant future work suggestions.

Chapter 2

Theoretical Review

Throughout this chapter, a brief theoretical review will be made, covering basic relations and assumptions on compressible flow around an airfoil, mostly derived from the thin airfoil theory.

Moreover, a quick introduction on turbulence models in a CFD context will be presented, as an attempt to give a background to the next chapters, due to the practical nature of the present work.

Finally, the model used in the simulations – the Spalart-Allmaras model – will be briefly explained in more detail. It is important to notice that the aim of this chapter is only to give a basic understanding of what was behind the CFD implementations, while it does not constitute a comprehensive guide on the analytical formulation for the theories presented.

2.1 - Compressible Flow Around an Airfoil

2.1.1 - Basic Relations

Compressible flows became a really important subject by the beginning of the 20th century, with the advent of high-speed flights, aerospace applications, military and ballistic studies and many other fields.

It is known that the compressibility of fluid starts to play a major role on the dynamics of a flow when the relative velocity of such fluid gets closer to the speed of sound. That is when changes on the density of a gas, for example, gets more relevant to the formulation, adding two more variables to the problem, density itself and temperature [13].

As a mechanical wave, the sonic velocity depends on the medium the wave travels. For ideal gases, it can be defined by equation (2.1).

$$a = \sqrt{\gamma RT} \tag{2.1}$$

Where a is the speed of sound, γ is the adiabatic index or ratio of specific heats (usually 1.4 for dry air), R is the specific ideal gas constant (for dry air, $287.058\,J/kg.K$) and T is the temperature of the fluid.

Another important relation in terms of the compressible flow formulation is the Mach number. The Mach number is a dimensionless quantity that represents the ratio between the flow velocity and the local speed of sound. Such relation can be seen in equation (2.2).

$$M = \frac{U}{a} \tag{2.2}$$

Where M is the Mach number (sometimes referenced as Ma) and U is the flow velocity.

Finally, the continuity equation expresses the conservation of mass, stating that the mass that flows through a system, considering the mass accumulation, is constant. The continuity equation can be seen in equation (2.3).

$$\frac{\partial \rho}{\partial t} + \frac{\partial \rho U}{\partial x} + \frac{\partial \rho V}{\partial y} + \frac{\partial \rho W}{\partial z} = 0 \quad or \quad \frac{\partial \rho}{\partial t} + \nabla.(\rho \vec{U}) \tag{2.3}$$

Where ρ is the fluid density, $\vec{U} = (U, V, W)$ is the velocity vector in $\vec{x} = (x, y, z)$ direction and t is time.

2.1.2 - Potential Flow

The compressible flow around an airfoil can be modelled assuming an inviscid and irrotational flow hypothesis. Consider a steady, irrotational and homentropic flow ($\nabla s = 0$, s being the entropy) where no forces are applied [14,15]:

$$\nabla.\left(\rho \vec{U}\right) = 0 \tag{2.4}$$

$$\nabla.\left(\frac{\vec{U}.\vec{U}}{2}\right) + \frac{\nabla P}{\rho} = 0 \tag{2.5}$$

$$\frac{P}{P_0} = \left(\frac{\rho}{\rho_0}\right)^{\gamma} \tag{2.6}$$

$$\nabla\left(\frac{P}{\rho}\right) = \left(\frac{\gamma - 1}{\gamma}\right)\frac{\nabla P}{\rho} \tag{2.7}$$

Where P is pressure and the index 0 denotes a ground level property.

Using the relation present in equation (2.7), it is possible to obtain a rearranged momentum equation as shown in equation (2.8).

$$\nabla\left[\left(\frac{\gamma}{\gamma-1}\right)\frac{P}{\rho}+\frac{\vec{U}.\vec{U}}{2}\right]=0 \tag{2.8}$$

Considering $\nabla P = a^2\nabla\rho$, and using it in the continuity equation in the form of equation (2.3) together with equation (2.7), the continuity equation becomes as presented in equation (2.9).

$$\vec{U}.\nabla a^2+(\gamma-1)a^2\nabla.\vec{U}=0 \tag{2.9}$$

In addition, the Bernoulli's equation in terms of freestream conditions is obtained and presented in equation (2.10).

$$\frac{a^2}{\gamma-1}+\frac{\vec{U}.\vec{U}}{2}=\frac{a_\infty^2}{\gamma-1}+\frac{U_\infty^2}{2}=\frac{a_\infty^2}{\gamma-1}\left(1+\frac{\gamma-1}{2}M_\infty^2\right)=C_pT_t \tag{2.10}$$

Where C_p is the heat capacity at constant pressure and T_t is the stagnation temperature. Moreover, the index ∞ represents the conditions at freestream.

Using equation (2.10), it is possible to state that:

$$\frac{a^2}{\gamma-1}=h_t-\frac{\vec{U}.\vec{U}}{2} \tag{2.11}$$

Where h_t stands for stagnation enthalpy.

Finally, the continuity equation is rearranged and with a little algebraic manipulation is presented in the form of equation (2.12).

$$(\gamma-1)\left(h_t-\frac{\vec{U}.\vec{U}}{2}\right)\nabla.\vec{U}-\vec{U}.\nabla\left(\frac{\vec{U}.\vec{U}}{2}\right)=0 \tag{2.12}$$

The equation (2.12) governs the compressible, steady, inviscid, irrotational motion relative to the velocity vector $\vec{U}$ [14,15].

Still, considering the irrotationality condition of $\nabla\times\vec{U}=0$ and the velocity in the potential form $\vec{U}=\nabla\phi$, the equation (2.12) can be rewritten as the equation (2.13).

$$(\gamma-1)\left(h_t-\frac{\nabla\phi.\nabla\phi}{2}\right)\nabla^2\phi-\nabla\phi.\nabla\left(\frac{\nabla\phi.\nabla\phi}{2}\right)=0 \tag{2.13}$$

The thin airfoil theory presented by both equations (2.12) and (2.13) is limited on its applicability, although numerical methods can be used to find a solution depending on the function ϕ. Thick airfoils or other bluff bodies only have analytical solution for small Mach number values (subsonic flows), before a shock region starts to appear. The shock occurring on supersonic flows at high Mach numbers invalidates the assumption of homentropic flow, making the theory not suitable for these cases [14].

2.1.3 - Small Disturbance Approximation and Linearized Formulation

A workaround to the problem of the model presented on section 2.1.2 which invalidates the solution for higher Mach numbers is achieved if the small disturbance theory is used. Such theory simplifies the equation (2.12), but still is only valid for thin airfoils.

Considerer a thin 3D airfoil or wing that only produces a small disturbance on the flow field. The velocity vector components would have now a small disturbance added to the freestream flow – equation (2.14).

$$\begin{cases} U = U_\infty + u \\ V = v \\ W = w \end{cases} \tag{2.14}$$

Where $u/u_\infty \ll 1$, $v/u_\infty \ll 1$ and $w/u_\infty \ll 1$.

The same assumption can be made to the state properties, adding a disturbance to the freestream condition as presented by equation (2.15).

$$\begin{cases} P = P_\infty + P' \\ T = T_\infty + T' \\ \rho = \rho_\infty + \rho' \\ a = a_\infty + a' \end{cases} \tag{2.15}$$

Thus, some common terms of equation (2.12) are now represented as follows:

$$\frac{\vec{U}.\vec{U}}{2} = \frac{U_\infty^2}{2} + uU_\infty + \frac{u^2}{2} + \frac{v^2}{2} + \frac{w^2}{2} \tag{2.16}$$

$$\nabla.\vec{U} = u_x + v_y + w_z \tag{2.17}$$

$$\nabla\left(\frac{\vec{U}.\vec{U}}{2}\right) = (u_x U_\infty + uu_x + vv_x + ww_x, u_y U_\infty + uu_y + vv_y + ww_y, u_z u_\infty + uu_z + vv_z + ww_z) \tag{2.18}$$

Substituting the terms from equations (2.16) – (2.18) in equation (2.12), neglecting third order and quadratic terms (excepting uu_x) in disturbance velocities, considering that $(\gamma - 1)\, h_\infty = a_\infty^2$ and dividing all the terms by a_∞^2, it is possible to obtain the simplified version of the continuity equation, as known as small disturbance equation presented in equation (2.19) [14,15].

$$(1 - M_\infty^2)u_x + v_y + w_z - \frac{(\gamma + 1)M_\infty}{a_\infty} uu_x = 0 \tag{2.19}$$

Potential velocity can be written as a summation of freestream and disturbance potential – $\phi = U_\infty x + \phi(x, y, z)$. Hence, the disturbance equation in terms of potential can be seen in equation (2.20).

$$(1 - M_\infty^2)\phi_{xx} + \phi_{yy} + \phi_{zz} - \frac{(\gamma + 1)M_\infty}{a_\infty} \phi_x \phi_{xx} = 0 \tag{2.20}$$

The equations (2.19) and (2.20) are valid for all Mach numbers range or all flow conditions: subsonic, transonic and supersonic, considering the initial assumptions are satisfied. However, it is possible to simplify even more those equations if the transonic state is ignored, as for Mach numbers far from one the nonlinear term can be neglected. The equation (2.20) reduces to the form shown in equation (2.21) [14,15].

$$\beta^2 \phi_{xx} - (\phi_{yy} + \phi_{zz}) = 0 \tag{2.21}$$

Being $\beta = \sqrt{M_\infty^2 - 1}$.

If the problem is only in two dimensions, the equation (2.21) simply becomes as presented in equation (2.22), known as the 2D linearized potential equation.

$$\beta^2 \phi_{xx} - \phi_{yy} = 0 \tag{2.22}$$

Lastly, the solution for equation (2.22) can be represented as the sum of two arbitrary functions F and G, as shown in equation (2.23).

$$\phi(x, y) = F(x - \beta y) + G(x + \beta y) \tag{2.23}$$

Depending on the values of M_∞^2, the equation (2.22) assumes the form of an elliptical function (if $M_\infty^2 < 1$, subsonic flow) or a hyperbolic function (if $M_\infty^2 > 1$, supersonic flow). In the first case, an analytical solution can be developed in terms of complex variables, while, in the second case, the solution is found as $x \pm \beta y = constant$ defines characteristic lines where the flow properties are constant [14,15].

2.1.4 - Lift and Drag Coefficients of Cambered Airfoils

For cambered airfoils, finding the analytical solution of lift and drag coefficients adds a few more levels of complexity. However, as being the most general case, only the solution for a thin cambered airfoil will be presented in this section.

Consider a thin cambered airfoil at a small angle of attack as presented in Figure 2.1. The displacement along y is represented by δ, the airfoil chord by c and the freestream Mach number by M_∞.

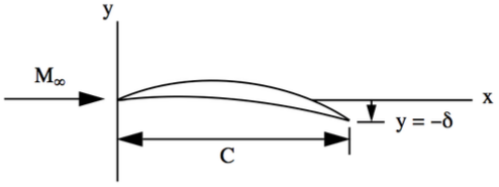

Figure 2.1 – Thin cambered airfoil at a small angle of attack representation [14].

The y-coordinate of the upper and lower surface is given by two functions f and g, as shown in equation (2.24) and (2.25), respectively.

$$f\left(\frac{x}{c}\right) = A\tau\left(\frac{x}{c}\right) + B\sigma\left(\frac{x}{c}\right) - \frac{\delta x}{c} \tag{2.24}$$

$$g\left(\frac{x}{c}\right) = -A\tau\left(\frac{x}{c}\right) + B\sigma\left(\frac{x}{c}\right) - \frac{\delta x}{c} \tag{2.25}$$

Where $2A/c \ll 1$ and $\delta/c \ll 1$, $\tau\left(\frac{x}{c}\right)$ is a dimensionless thickness function ($\tau(0) = \tau(1) = 0$) and $\sigma\left(\frac{x}{c}\right)$ is a dimensionless camber function ($\sigma(0) = \sigma(1) = 0$).

Considering the relation $\tan\alpha = -\delta/c$ for the angle of attack α, the small angle assumption with $\cos\alpha = 1$ and that $\xi = x/c$ for simplification purposes, the lift coefficient, from the lift integral, can be written accordingly to equation (2.26) .

$$C_L = \frac{L}{\frac{1}{2}\rho_\infty U_\infty^2 c} = \int_0^1 C_{P_{lower}} d\xi - \int_0^1 C_{P_{upper}} d\xi \tag{2.26}$$

Where C_L is the lift coefficient, L is the lift force and $C_{P_{lower}}$ and $C_{P_{upper}}$ are the pressure coefficients of the lower and upper surface, expressed by equations (2.27) and (2.28), respectively.

$$C_{P_{lower}} = -\frac{2}{c\sqrt{M_\infty^2 - 1}}\left(\frac{dg}{d\xi}\right) = -\frac{2}{c\sqrt{M_\infty^2 - 1}}\left(-A\frac{d\tau}{d\xi} + B\frac{d\sigma}{d\xi} - \delta\right) \tag{2.27}$$

$$C_{P_{upper}} = \frac{2}{c\sqrt{M_\infty^2 - 1}}\left(\frac{df}{d\xi}\right) = \frac{2}{c\sqrt{M_\infty^2 - 1}}\left(A\frac{d\tau}{d\xi} + B\frac{d\sigma}{d\xi} - \delta\right) \tag{2.28}$$

Substituting equations (2.27) and (2.28) in equation (2.26), the lift coefficient becomes as presented in equation (2.29).

$$C_L = \frac{-2}{c\sqrt{M_\infty^2 - 1}}\int_0^1 \frac{df}{d\xi} d\xi + \int_0^1 \frac{dg}{d\xi} d\xi = \frac{-2}{c\sqrt{M_\infty^2 - 1}}\int_0^{-\delta} df + \int_0^{-\delta} dg \tag{2.29}$$

Using the thin airfoil assumption, it is possible to approximate the equation (2.29) by making it independent of the thickness, as seen in equation (2.30) [14,15].

$$C_L = \frac{4}{\sqrt{M_\infty^2 - 1}}\left(\frac{\delta}{c}\right) \tag{2.30}$$

Similarly, the drag coefficient C_d can be obtained from the drag integral using the same assumptions of the thin airfoil theory at small angles of attack. Making some algebraic manipulations, the drag coefficient can be expressed as in equation (2.31).

$$C_d = \frac{D}{\frac{1}{2}\rho_\infty U_\infty^2 c} = \frac{1}{c}\int_0^1 C_{P_{upper}}\left(\frac{dy_{upper}}{d\xi}\right) d\xi \;\; + \frac{1}{c}\int_0^1 C_{P_{lower}}\left(-\frac{dy_{upper}}{d\xi}\right) d\xi \tag{2.31}$$

Substituting the expressions for the pressure coefficients – equations (2.27) and (2.28) – and making the necessary manipulations, the drag coefficient becomes as presented in equation (2.32) [14,15].

$$C_d = \frac{4}{\sqrt{M_\infty^2 - 1}}\left[\left(\frac{A}{c}\right)^2 \int_0^1 \left(\frac{d\tau}{d\xi}\right)^2 d\xi + \left(\frac{B}{c}\right)^2 \int_0^1 \left(\frac{d\sigma}{d\xi}\right)^2 d\xi + \left(\frac{\delta}{c}\right)^2 \int_0^1 d\xi\right] \tag{2.32}$$

The expression for the drag coefficient shown in equation (2.32) can be interpreted as a sum of drags originated from thickness, camber and lift [14].

All the formulation presented in this section gives a basic background on how some important parameters such as lift and drag coefficients used to be calculated and anticipated in the early stages of the development of transonic and supersonic flights. Before supercomputers made possible the implementation of much more complex problems, aerospace engineers relied mainly in these similarity models and wind tunnels validations to design their projects [14]. This section only represents a reference and is far from being extensive on the subject, as the present work used modern computational methods and tools mostly based on turbulence models. A brief discussion on turbulence models is presented in section 2.2.

2.2 - Turbulence Models

When it comes to high-speed flows (and most nature phenomena), turbulence plays a major role. It is possible to observe a turbulent flow occurring on a daily basis, as smoke coming out of a chimney, water flowing in a river and wind blowing intensively are perfect examples of how a flow can be unsteady, chaotic and seemingly random [16].

It is possible to classify a flow as turbulent depending on a specific dimensionless parameter, the Reynolds number. The Reynolds number is defined in equation (2.33).

$$Re = \frac{\rho u L}{\mu} = \frac{uL}{\nu} \tag{2.33}$$

Where μ is the dynamic viscosity of the fluid, ν is the kinematic viscosity of the fluid and L is a characteristic length.

Although there is not an exact Reynolds number for when a flow becomes turbulent as it depends on the nature of the problem (in a circular pipe flow, for example, this value is around $Re_D = 4{,}000$ for fully-developed turbulence, and in boundary layer problems, around $Re_x = 100{,}000$), higher Reynolds numbers usually indicate that turbulence is occurring [17].

Despite the unpredictable nature of turbulent flows, the phenomenon of turbulence is accurately described by the Navier-Stokes equations. These equations, using indexes to

represent the components and the Einstein's notation[2], can be seen in equation (2.34) in the most general formulation.

$$\rho\left(\frac{\partial U_j}{\partial t}+U_i\frac{\partial U_j}{\partial x_i}\right)=\rho g_i-\frac{\partial P}{\partial x_j}-\frac{\partial \tau_{ij}}{\partial x_i} \tag{2.34}$$

Where g is gravity acceleration and τ is the stress tensor.

These set of equations, together with the continuity equation, equation (2.3), is the most important mathematical model of the fluid dynamics. However, there are only a few applications where it is possible to find an analytical solution for them. Due to its complexity, turbulent flows do not have a way to be explicitly solved without relying on numerical methods and formulations, and even then, the capacity of solving most problems directly is limited [16].

In this context, several turbulence models have been developed over the years trying to overcome these limitations. As any other numerical model, each one has an application and a core motivation that originated its formulation. In terms of classification, the turbulence models can be roughly divided into two main groups: direct and statistical methods. A brief discussion on the most important models are presented in the next subsections.

2.2.1 - DNS

Direct Numerical Simulation or DNS, as the name indicates, is a direct method that consists in solving the Navier-Stokes equations – equation (2.34) – in order to determine the instantaneous velocity field [16]. All scales of motion are resolved using DNS and each simulation only produces a single realization of the flow.

It is the simplest approach, which brings the most accuracy and an unparalleled level of description of the motion, but as one can expect, the computation cost of such task is huge. The requirements increase so rapidly depending on the Reynolds number, that the method itself was infeasible until more advanced computers were introduced [16]. To this day, DNS still has a more academic application, as its implementation is not practical for industrial flows. In Figure 2.2, it is possible to see a DNS result for a generic flow (only for comparison purposes).

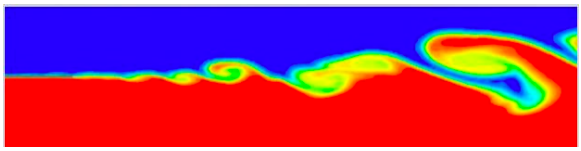

Figure 2.2 – DNS result for a generic flow [18].

[2] Einstein's notation is way to represent complex equations by suppressing the summation symbol. The notation assumes that a repeated index within a term is equivalent to the summation itself. For example, $\frac{\partial a_i}{\partial x_i} \rightarrow \sum \frac{\partial a_i}{\partial x_i}$.

2.2.2 - LES

The Large-eddy Simulation (LES) is a hybrid method where larger three-dimensional turbulent flows are calculated directly, and smaller motions are modelled by a different approach [16].

First introduced by Smagorinsky [19] for meteorological studies, the method is increasingly being used on several other complex applications and producing good results, although meteorological and atmospheric boundary layers still remain the main focus of LES [16]. In terms of computational cost, it is not the most efficient formulation available, however it produces a great level of accuracy for certain problems at a reasonable computational expense if compared to DNS, by avoiding explicit small-motions calculations.

An important part of LES is filtering the motion, where the velocity is decomposed into the sum of a filtered or resolved component and a residual component. This way, the large-eddy motion (filtered velocity) can be calculated by the standard form of the Navier-Stokes equations – equation (2.34), including the residual stress-tensor in the momentum equation. This last one is modelled in a simpler way, usually by an eddy-viscosity model [16].

Again, as any other numerical method, there are several other variations of LES that have been developed over the years for a wide range of applications, such as LES including near-wall resolution (LES-NWR), including near-wall modelling (LES-NWM) or very large-eddy simulation (VLES). These variations usually change the filtering parameters and the grid size, affecting on how the energy will be calculated throughout the mesh [16]. In Figure 2.3, it is presented a generic case output obtained with LES. Comparing it to Figure 2.2, it is possible to realize some differences, especially in the resolution of the smaller motions representation.

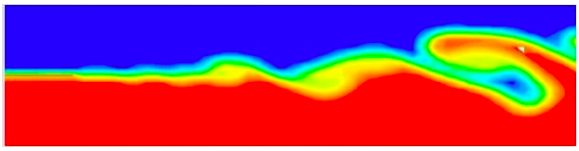

Figure 2.3 – LES result for a generic flow [18].

2.2.3 - RANS

Reynolds Averaged Navier-Stokes Simulations, RANS, are by far the most used approach in industry applications. By definition, it is considered a variety of statistical methods, as time-averaged variables are used to solve the Reynolds averaged Navier-Stokes equations.

A lot of different hypotheses were constructed using the time-averaged and fluctuating quantity approach, firstly proposed by Osbourne Reynolds himself. For example, some methods use the turbulent-viscosity hypothesis, while others rely on a more directly formulation derived from the Reynolds-stress transport equations.

As extensive as the subject is, some well-known and most used RANS models available on commercial computational tools are:

- One-equation: Spalart-Allmaras model. Developed for aerospace applications, this one-equation model converges to a solution using the kinematic eddy turbulent viscosity assumption [20]. Despite the fact that it is quite economical for large meshes, it does not perform in a satisfactory way for there-dimensional cases (more on this model in the section 2.3, as it was the one used in the implementations of the present work);
- Two-equations: $\kappa - \epsilon$ model. Relying on the kinetic (κ) and dissipation of turbulence energy (ϵ) transport equations, together with a specification for the turbulent viscosity, it is the most used complete model available in CFD tools. From the two quantities, a lengthscale, a timescale and a quantity of dimension can be formed, in a way that flow dependent specifications are no longer required [16]. The computational cost of the $\kappa - \epsilon$ model is highly optimized for most applications, making it the preferable method of many engineers and designers;
- Two-equations: $\kappa - \omega$ model. The difference between this model and the $\kappa - \epsilon$ is that the diffusion term of the first formulation is supressed by using ω, the specific rate of dissipation. This makes the $\kappa - \omega$ model superior for boundary layer flows, considering near-wall viscous treatment and the streamwise pressure gradient effects. However, non-turbulent freestream boundaries must be treated with caution when utilizing this model [16];
- Reynolds-stress models. In these models, the transport equations are modelled for the individual Reynolds stresses and for the dissipation, in a way that the turbulent viscosity hypothesis is not required [16]. It provides more accurate results, in the expense of a higher computational cost, if compared to the other methods presented in this subsection. Due to these characteristics, it suits 3D complex geometries better, ones that require an extensive analysis of strong curvatures or swirl motions.

In Figure 2.4, it is possible to observe the same generic case resulted from a RANS CFD implementation. Comparing the outputs, it is evident that a simpler flow representation is obtained, but, for most of the cases, especially in engineering, such results are sufficient to describe the main relevant phenomena.

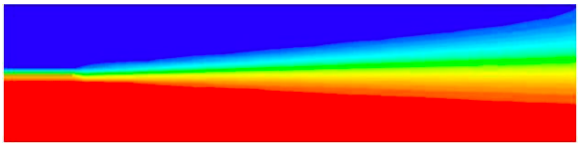

Figure 2.4 – RANS result for a generic flow [18].

The models presented in this section are only a small sample of many others available on the RANS category. Many models have evolved or have been developed over the years, so even a complete list now is not a definite set of everything available on the subject.

2.3 - Spalart-Allmaras Model: A Summary

The turbulence model used in the present work was the Spalart-Allmaras. As briefly discussed in the last section, this model was developed for aerospace applications and suited the implementation of the cavity in this present work due to its characteristics: 2D geometry in a transonic state with flow separation.

A good convergence and a fairly robust implementation for the studied problem were considered and helped choosing the Spalart-Allmaras model as final method in the cavity analysis and all simulations performed.

2.3.1 - Formulation

The model is a one-equation formulation for eddy viscosity ν_t, by a viscosity-dependent parameter $\tilde{\nu}$, and is presented in equation (2.35), with the parameters defined in equations (2.36) – (2.38) [20].

$$\frac{\partial \tilde{\nu}}{\partial t} + u_j \frac{\partial \tilde{\nu}}{\partial x_j} = c_{b1}(1 - f_{t2})\tilde{S}\tilde{\nu} - \left[c_{w1} f_w - \frac{c_{b1}}{\kappa^2} f_{t2}\right]\left(\frac{\tilde{\nu}}{d}\right)^2 + \frac{1}{\sigma}\left[\frac{\partial}{\partial x_j}\left((\nu + \tilde{\nu})\frac{\partial \tilde{\nu}}{\partial x_j}\right) + c_{b2}\frac{\partial \tilde{\nu}}{\partial x_i}\frac{\partial \tilde{\nu}}{\partial x_i}\right] \quad (2.35)$$

$$\nu = \tilde{\nu} f_{v1} \qquad f_{v1} = \frac{\chi^3}{\chi^3 + c_{v1}^3} \qquad \chi = \frac{\tilde{\nu}}{\nu} \quad (2.36)$$

$$f_{v2} = 1 - \frac{\chi}{1 + \chi f_{v1}} \qquad f_w = g\left[\frac{1 + c_{w3}^6}{g^6 + c_{w3}^6}\right]^{\frac{1}{6}} \qquad \tilde{S} = \Omega + \frac{\tilde{\nu}}{\kappa^2 d^2} f_{v2} \quad (2.37)$$

$$g = r + c_{w2}(r^6 - r) \qquad r = min\left[\frac{\tilde{\nu}}{\tilde{S}\kappa^2 d^2}, 10\right] \qquad f_{t2} = c_{t3}\, e^{(-c_{t4}\chi^2)} \quad (2.38)$$

Where Ω is the vorticity magnitude expressed by $\Omega = \sqrt{2W_{ij}W_{ij}}$, being d the distance from the field point to the nearest wall and $W_{ij} = \frac{1}{2}\left(\frac{\partial u_i}{\partial x_j} - \frac{\partial u_j}{\partial x_i}\right)$.

The boundary conditions were defined as the set of equations shown in equation (2.39).

$$\tilde{\nu}_{wall} = 0 \quad and \quad \tilde{\nu}_{farfield} = 3\nu_\infty : to : 5\nu_\infty \quad (2.39)$$

Where the $wall$ and $farfield$ indexes indicate the region where the boundary condition applies.

2.3.2 - Constants

Relying on several experimental methods, many constants were defined in the model as a way to adjust the outcome. The Table 2.1 brings these constants values [20], which are directly used in equations (2.35) – (2.38).

Table 2.1 – Spalart-Allmaras model constants.

Constant	Value	Constant	Value
σ	$\frac{2}{3}$	c_{t3}	1.2
κ	0.41	c_{t4}	0.5
c_{b1}	0.1355	c_{w1}	$\frac{c_{b1}}{\kappa^2}+\frac{1+c_{b2}}{\sigma}$
c_{b2}	0.622	c_{w2}	0.3
c_{v1}	7.1	c_{w3}	2

The incorporation of these constants in the formulation makes the model adjustable to certain conditions. Some modifications to the original formulation have already been proposed in order to ensure good convergence depending on the problem [21–25].

As one can infer, the model itself is far more complex than what was presented here, and this summary does not contemplate many nuances, nor the complete math proposed by the original publication referenced throughout this section. Due to the practical nature of the present work, this serve only as quick background on the subject, while the implementation used on the calculations was already available in the commercial software chosen to obtain the results.

2.4 - Conclusion

This chapter presented a brief discussion on the theory and models behind the study of a flow around an airfoil.

First, an analytical approach was presented to show how researchers used to rely on approximations and experimental data to design many important parameters of a flight. Having no practical application nowadays with the use of CFD tools for most calculations, an overview of turbulence models was presented next, in order support and give a background to the chapters to come. Finally, the chosen model (Spallart-Allmaras model) for the analyses discussed in the present work was summarized, with basic formulation and constants presented as a quick reference.

Chapter 3

Methodology

The sections of this chapter bring the most important parameters and settings used in the simulations of the present work. As a CFD-based project, here is presented the core elements that made possible obtain the results that will be discussed in Chapter 4.

First, a basic project outline will be shown to give an idea of how the present work was divided and organized, in order to reach its objectives. Afterwards, the geometries of the airfoil (standard and modified) will be presented, leading to how the mesh was obtained and optimized to the simulations to come.

Finally, the boundary conditions will be discussed, exploring how the settings were defined to make possible comparisons with the literature.

3.1 - Project Outline

In order to evaluate the cavity effect on the airfoil NACA 4412 and facilitate the working process, the present work was divided in several steps, from defining the geometry and the type of airfoil to be used, to implementing the cavity cases and analysing the final results.

It is important to notice that the software used in all implementations and post-processing was comprehended in the ANSYS® Workbench™ package, being the CFD simulations performed in the ANSYS® Fluent® environment. Due to the work extension, all cases were run in a computer cluster, where a Linux® version of the software was previously installed. The computational infrastructure was gracefully provided by Brunel University London to support the present work.

In Figure 3.1 it is possible to see the project outline and the several steps performed during the cavity effect study.

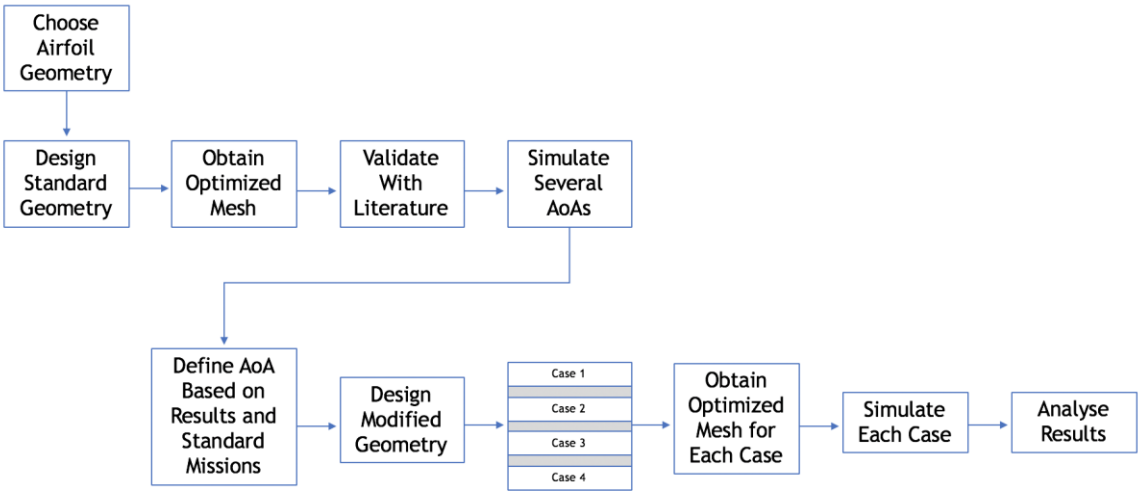

Figure 3.1 – Project outline.

All the steps shown in Figure 3.1 pass a general idea of workflow for the present work. Many other processes involved in the project were omitted due to relevance and to make the diagram more concise. As one can see, a whole analysis of the standard NACA 4412 airfoil in several angles of attack were performed prior to the simulation of the cavity cases itself. This important step made possible many adjustments in the implementation, leading to a more precise approach of the modified airfoil study. As a unique work, many simulations were performed repeatedly and altered until consistent results were obtained. In the next sections, many aspects of the steps presented in Figure 3.1 will be discussed more deeply.

3.2 - Geometry

The first step of the present work was to determine which airfoil best suited the project objectives. A good starting point was to evaluate the airfoils used in the EUROSHOCK programmes [10,11], however, as being mostly proprietary models, it would made access to design and experimental data more difficult.

In this context, a different approach was taken and, in order to reduce the overhead of the project, the airfoil NACA 4412 was chosen. The main reasons that motivated this choice was:

1. One of the most common airfoil profiles with well-established experimental data available in the literature;
2. A cambered profile, which reduces the symmetry influence on the results;
3. Reasonably simple geometry, reducing design effort and potential computational issues;
4. Real application in commercial aircrafts.

The NACA 4412 is part of the so-called four-digit NACA series airfoils, where each digit (or pair of digits) specifies a design parameter of the airfoil. That way, the first digit indicates

the maximum camber (m) in percentage of chord or airfoil length (c), the second represents the position of such maximum camber (p) in tenths of chord and the last two digits provide the maximum airfoil thickness (t) in percentage of chord [26]. Thus, the design parameters of NACA 4412 airfoil can be found in Table 3.1.

Table 3.1 – Design parameters of NACA 4412 airfoil.

Parameter	Value [% of c]
Maximum Camber (m)	4%
Maximum Camber Position (p)	40%
Maximum Thickness (t)	12%

In Figure 3.2, a basic diagram of NACA 4412 airfoil is displayed to show how the design parameters presented in Table 3.1 are defined within the geometry.

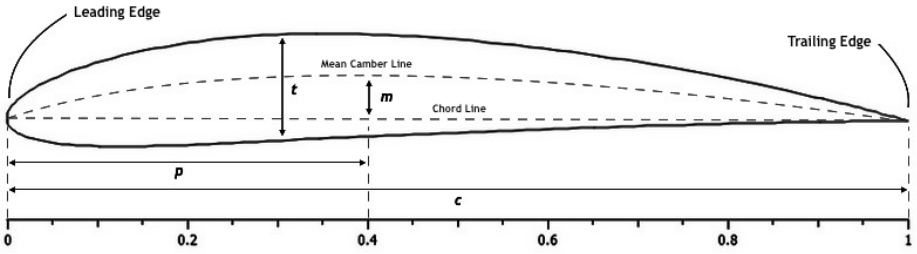

Figure 3.2 – NACA 4412 design parameters diagram.

It is important to notice that the diagram in Figure 3.2 is just illustrative and does not maintain real dimensions and scale. In addition, even though it already represents the NACA 4412 geometry, it can be used as reference for all four-digit NACA series airfoils.

As stated before, one of the premises of choosing the NACA 4412 profile was to be an airfoil with real commercial aircraft applications. In this matter, NACA 4412 is widely used in many airplane models, usually light, single-engine ones. A popular example is the Citabria Explorer, manufactured by American Champion Aircraft Corporation, mostly used for flight training, utility and even acrobatics purposes [27].

Although the flow in these types of aircraft are essentially subsonic, the study of a more general airfoil with commercial applications constitutes a great stepping-stone to future analyses, as the main focus of the present work was to study how the secondary flow generated by the cavity implementation influenced the main flow in terms of separation and drag and lift coefficients.

In Figure 3.3, it is possible to see the Citabria Explorer. One can notice right away the NACA 4412 profile used on the wings.

Figure 3.3 – Citabria Explorer with NACA 4412 profile on the wings [27].

Moreover, another important definition made in the beginning of the present work was if the implementation would be in two or three dimensions. It is known that a 3D implementation would approximate the problem even more to the reality, but in terms of physical meaning could not add that much. Thus, by opting for symmetry planes on a typical case of infinity wing, a 2D study could focus on the effect of the cavity itself, reducing the computational cost of the simulations and avoiding unnecessary design complexity. This conclusion was made based on preliminary 3D studies implemented in the early stages, here omitted for not being part of the present work scope. Therefore, all the study performed in the present work was made considering 2D cases for both standard and modified NACA 4412 airfoils.

3.2.1 - Standard Airfoil

In order to implement the standard airfoil, the design points were obtained in the literature and sketched with the aid of the ANSYS® DesignModeler™ tool. These design points are easily calculated by functions defined in the NACA four-digit airfoil series conception itself [26].

In Figure 3.4, it is shown the final design used for the standard airfoil simulations.

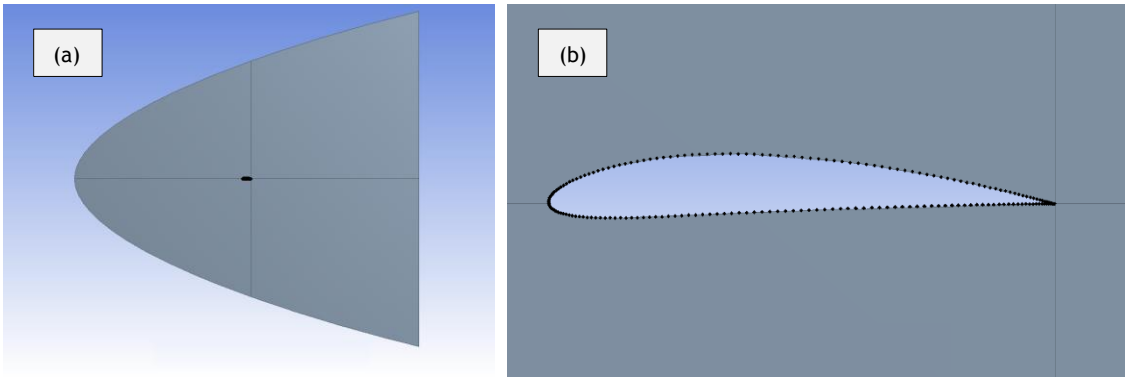

Figure 3.4 – NACA 4412 standard geometry, a) enclosure overview and b) detailed view of the airfoil.

From Figure 3.4, it is possible to see that the enclosure was designed as a parabolic C-shape divided into four different sections or faces. This measure was taken to help the mesh process and to make the simulation more efficient, as will be discussed in section 3.3.

The presence of an enclosure itself is necessary as it works as boundaries to the external flow simulation, as long as it is sufficient large to act as freestream and avoid the interference of the object in the boundary conditions. In the end, the software considers the enclosure as final geometry, being the airfoil subtracted from the surface, in a sort of "negative" or "cast" kind of setting. The Table 3.2 brings the main sizes of the enclosure and of the airfoil.

Table 3.2 – Main geometry sizes of standard and modified airfoils.

Parameter	Value [unit]
Airfoil Chord (c)	$1\ [m]$
Enclosure Total Length	$41\ [m]$
Enclosure Maximum Height	$40\ [m]$

It is important to notice that the values presented in Table 3.2 was used in both sets of simulations, the standard and modified airfoil cases. Moreover, the enclosure was configured in a way that the boundaries would be placed approximately $20\,m$ far from the airfoil in each direction (20 times the airfoil chord). This enclosure size has shown to be more than sufficient [28], not interfering in the results presented in Chapter 4. In addition, the chord was defined as unity to simplify eventual further calculations

Finally, as stated before, the four sections or faces of the surface were defined by the x and y axes, being the origin placed in the airfoil trailing edge. The airfoil was designed according to a zero-degree orientation for the angle of attack, as showed in Figure 3.4.

3.2.2 - Modified Airfoil: Cavity Implementation

The modified airfoil geometry was totally based on the standard case, which minimized the design effort for the cavity study. As the fully developed cavity case was not studied in the present work, each cavity linked by the internal channel was treated as "semi-cavity", only for clarification purposes.

However, first these semi-cavities positions had to be defined considering the standard airfoil simulations (discussed in full in Chapter 4). The cavity study was divided into four cases, each one corresponding to a different approach. The first two considered both semi-cavities with length increments, to equalize the discharge velocity upstream:

1. Shock occurring above the upstream semi-cavity, both semi-cavities with length increments towards the centre;
2. Shock occurring between semi-cavities, both semi-cavities with length increments towards the centre.

In Figure 3.5, it is possible to see diagrams for the first two cases. In the diagrams, the shock and the secondary flow are also represented.

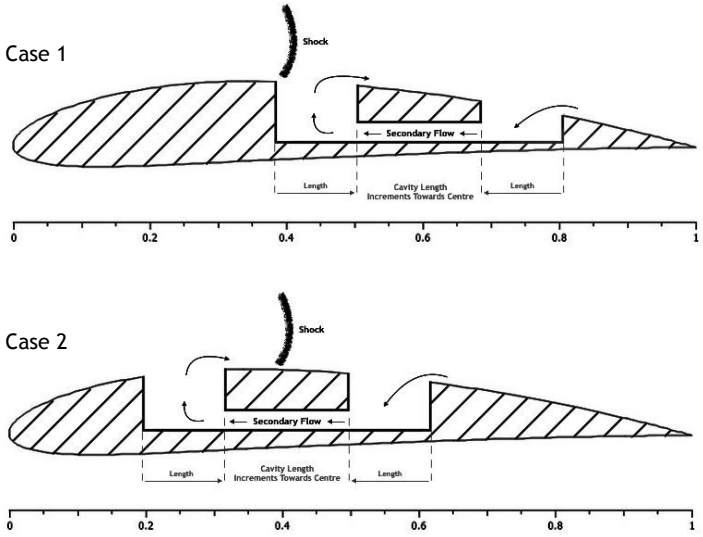

Figure 3.5 – NACA 4412 modified geometry diagrams, cases 1 and 2.

The last two cases considered a fixed length for the upstream semi-cavity, in order to control the suction effect downstream and evaluate how this would influence the lift and drag coefficients. This are represented in Figure 3.6. The cases are described as follows:

3. Shock occurring above the upstream semi-cavity, just downstream semi-cavity with length increments towards the other semi-cavity;
4. Shock occurring between semi-cavities, just downstream semi-cavity with length increments towards the other semi-cavity.

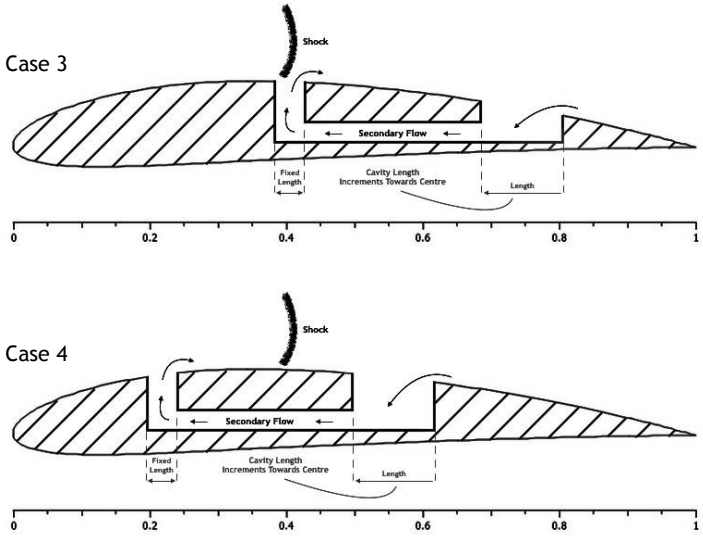

Figure 3.6 – NACA 4412 modified geometry diagrams, cases 3 and 4.

These four different approaches considered the shock location and the pressure distribution obtained from the standard simulations as decisive parameters to place the cavity and were inspired by the experiments performed in the context of the EUROSHOCK programmes [10,11].

In order to maintain a method that could lead to an unbiased analysis, all other cavity-related geometric parameters were kept constant, such as maximum depth, channel height and total length, being the semi-cavity length the only variable, according to what was proposed in each case. The Table 3.3 brings the main geometric parameters of the cavity, the length range used in each case (in the form of INITIAL_LENGTH:STEP:FINAL_LENGTH) and the cavity positions in percentages of the airfoil chord.

Table 3.3 – Main geometric parameters of the cavity cases.

Case	Parameter	Value [unit]
All Cases	Cavity Total Length	$425\ [mm]$
	Maximum Cavity Depth	$90\ [mm]$
	Channel Height	$25\ [mm]$
Case 1 and 2	Upstream Semi-Cavity Length	$50{:}\,25{:}\,200\ [mm]$
	Downstream Semi-Cavity Length	$50{:}\,25{:}\,200\ [mm]$
Case 3 and 4	Upstream Semi-Cavity Length (Fixed)	$50\ [mm]$
	Downstream Semi-Cavity Length	$50{:}\,50{:}\,350\ [mm]$
Case 1 and 3	Beginning of Cavity	37.5%
	End of Cavity	80%
Case 2 and 4	Beginning of Cavity	18.75%
	End of Cavity	61.25%

Finally, in Figure 3.7, it is possible to see the final design used in the modified airfoil simulations. Again, a full analysis of the shock location will be made in Chapter 4, as its determination was obtained as result of the standard airfoil simulations for the chosen angle of attack.

It is important to notice that in Figure 3.7, it is only represented the first configuration of the cases 1-3 and 2-4. As seven lengths were tested for each case, the subsequent geometries were omitted to keep the text more fluid.

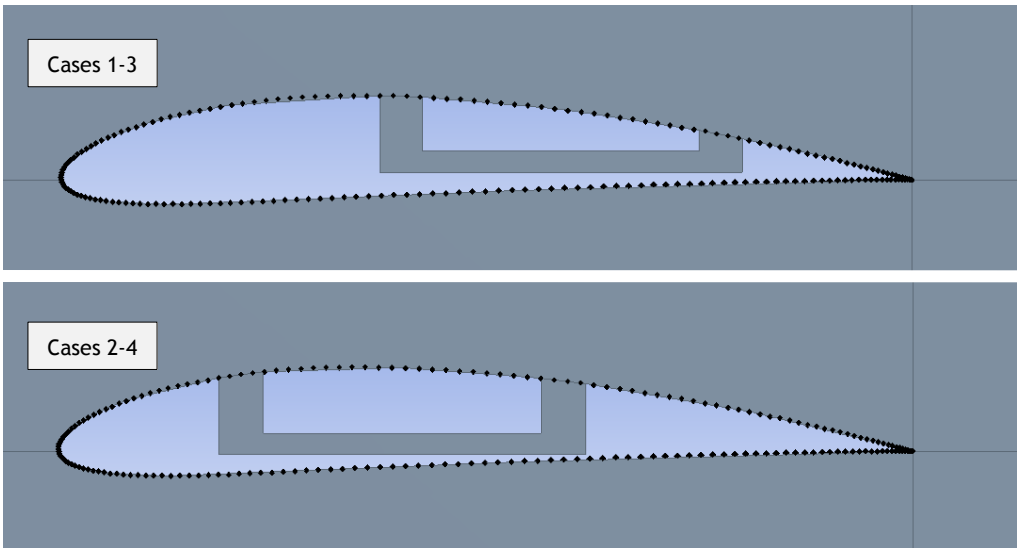

Figure 3.7 – NACA 4412 modified geometries, initial configuration for cases 1-3 and 2-4.

With the geometries for both standard and modified airfoils determined, the next step was to obtain the model meshes, as will be discussed in the section 3.3.

3.3 - Mesh

Meshing the model is undoubtedly one the most important steps in any CFD simulation. A good mesh provides more accurate results, reducing the discretization error intrinsic to all numerical methods.

However, establishing a good mesh is not an easy task. There are many indicators and statistics to support and help the designer on the matter, such as refinement (element size), element skewness, orthogonality and aspect ratio, for instance. Ideally, the finer the mesh, the better, but there is always a trade-off between computational cost and level of refinement, and sometimes a finer grid can influence the results depending on the turbulence model used in the simulations. Thus, the main goal is always to find this balance, knowing what to expect in terms of physical meaning and keeping in mind the numerical method characteristics. In the end, a good mesh should provide consistent results, preferably reaching a level where they are considered mesh-independent (when improving the mesh quality will not influence the results anymore).

Therefore, several different approaches were taken in the present work in order to obtain final quality grids for the simulations to come. In each step, the complexity and the quality of the meshes increased, resulting in grids with specifications in accordance to general guidelines for the model used, to the literature and validated via comparison with experimental data. Many attempts were made, even with 3D geometries, but only the most important three will be discussed in the following subsections, being the last one used as the final mesh for the present work. The conditions used in the attempts were the same ones

presented in section 3.4, with angle of attack of zero degrees. It is important to notice that all the meshes used in the context of this project were generated by the ANSYS® Meshing™ tool, as it is the only tool for mesh generation available in the more recent versions of ANSYS® Workbench™ package. Although there is a plethora of other options in terms of meshing tools, the level of integration between ANSYS® Meshing™ and ANSYS® Fluent® reduced the effort and potential problems due to incompatibility during the simulation phase.

3.3.1 - Unstructured Mesh

The first approach in order to obtain a quality mesh for the cases studied in the present work was to generate an unstructured mesh. An unstructured mesh is usually easier to obtain, as it relies mostly in the algorithm available in the meshing tool. This algorithm has the premise to randomly distribute elements (triangles, quadrilaterals or hybrid) in the computational space, making the process much more automatic and suitable for complex geometries [29].

Moreover, the moderate computational expense of the process and the flexibility in terms of adaptive meshing also provides a great plus [29]. Being a cambered airfoil, in addition to a cavity in the next step of the project, the unstructured mesh seemed a good starting point.

In Figure 3.8, the first mesh attempt with an unstructured grid is presented.

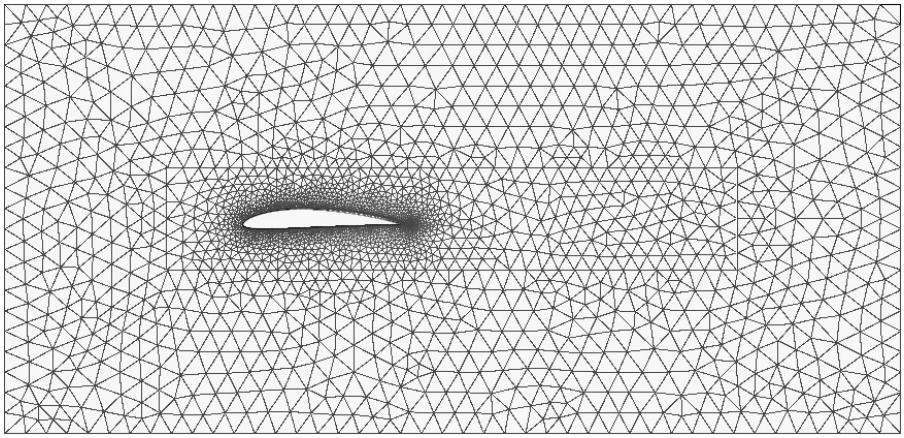

Figure 3.8 – Unstructured mesh for standard airfoil geometry.

From Figure 3.8, it is possible to see that the elements were mainly formed by triangles and an inflation method was imposed near the wall to capture the phenomena more accurately in the region close to the airfoil. Furthermore, in order to keep as simple as possible, the enclosure used was a two-section rectangle, which has proven not to be ideal for the problem studied.

Despite the fact that the mesh obtained produced great statistical indicators (skewness, orthogonal quality and aspect ratio), as it was an automatic software-controlled process, preliminary results showed several problems in regard to the shape of the enclosure influencing the flow and the dynamics near the wall. This was sufficient to search for another solution in terms of mesh, without further implementations.

The Table 3.4 presents a summary of the motivations, qualities and flaws of the unstructured mesh given the problem studied.

Table 3.4 – Summary of unstructured mesh attempt for the studied geometries.

Unstructured Mesh Attempt	
Motivation	Quick method with low user interaction, moderate computational cost and capable of producing good results.
Qualities	Automatic and robust, software-controlled and high adaptive capability in complex geometries.
Why Not Suitable?	Results were not as expected near the wall even with inflation, enclosure shape influenced the flow.

3.3.2 - Structured C-Shape with Rectangular Section

After the unstructured mesh, a much more advanced approach was taken. First, the enclosure shape was modified to a C-shape geometry, with a rectangular section. Second, the mesh itself was designed as a structured quadrilateral grid.

In this context, a structured grid demands much more design time as several parameters must be defined manually in order to organize the elements around the geometry, especially complex ones, but sometimes this reduces the simulation computational cost. Furthermore, it is known that structured grids converge better in certain conditions and produce more accurate results in terms of aerodynamic parameters, such as lift and drag coefficients [30,31]. This alone represented a great motivation to invest in a structured mesh.

In Figure 3.9, it is shown the structured C-shape with rectangular section mesh, another attempt to establish a final mesh for the present study.

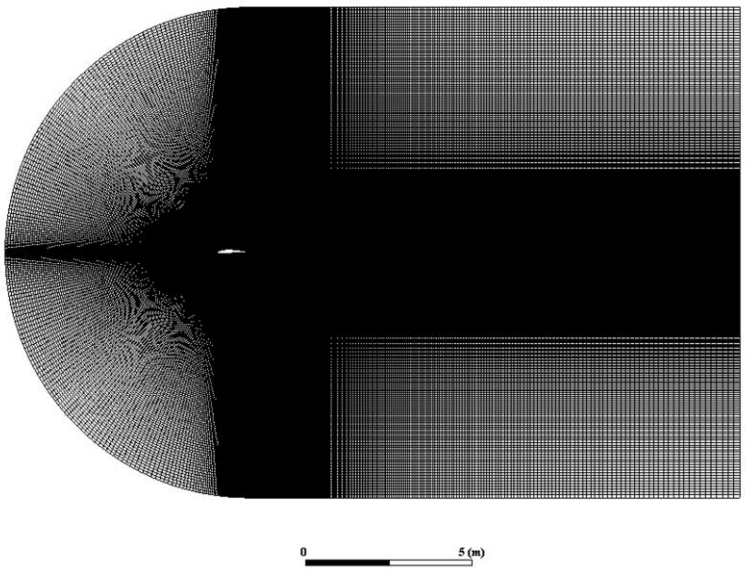

Figure 3.9 – Structured C-shape/rectangular mesh for standard airfoil geometry.

It is possible to see in Figure 3.9 that the mesh was configured to be much finer in strategic places, especially in the area close to the airfoil. The grid is so refined in this area, that is impossible to see a single element in this overview representation.

Despite NACA 4412 airfoil not being the simplest or symmetrical geometry, it does not constitute a prohibitive factor to generate a structured mesh either. Moreover, a structured grid is usually formed by elements with more quality and makes the boundary layer analysis more accurate, as the elements are mostly aligned with the flow. In addition, it is possible to assess and control y^+ (dimensionless wall distance) values more easily, an important parameter to wall-bounded flows (like the flow around an airfoil, subject of the present work) and relevant to certain turbulence models. In Figure 3.10, two detailed views show the mesh near the airfoil wall.

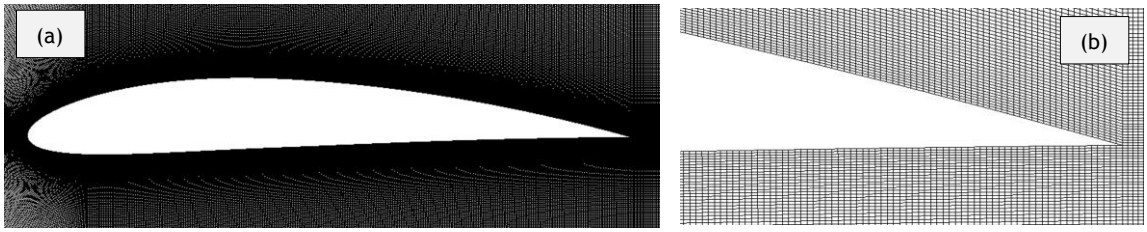

Figure 3.10 – Structured C-shape/rectangular mesh for standard airfoil geometry, detailed views of a) whole airfoil and b) trailing edge.

Even in the detailed views shown in Figure 3.10, it is difficult to see a single element size near the wall. This level of refinement produced great mesh metrics for the $802{,}000$ elements present on the grid, as can be seen in Table 3.5.

Table 3.5 – Mesh metrics for the structured C-shape/rectangular grid, standard airfoil.

Parameter	Minimum	Maximum	Average
Skewness	1.3057×10^{-10}	0.60892	3.0748×10^{-2}
Orthogonal Quality	0.581	1	0.99571
Aspect Ratio	1.0005	240	10.637

It is important to notice from Table 3.5 that for skewness, the closer the values are to zero, the better, while for the orthogonal quality it is the inverse, values closer to unity usually represents a better mesh. The high values for aspect ratio come from the sharp trailing edge, that generated some distorted elements downstream. However, being far from the airfoil and the main flow, that did not influence the results.

After preliminary tests were run, some problems with the mesh started to appear. When the angle of attack was zero, the results were consistent and comparable to the literature. For other angles though, the solution struggled to converge in terms of residuals and statistically for drag and lift coefficients. The probable main reason for this situation was the

discontinuity in the domain caused by the rectangular section of the geometry. Thus, a further step was taken to address this problem by changing the boundary shape, as will be discussed in subsection 3.3.3. The Table 3.6 shows the summary for the referred mesh attempt.

Table 3.6 – Summary of structured C-shape/rectangular mesh attempt for the studied geometries.

Structured C-Shape/Rectangular Mesh Attempt	
Motivation	Better results for aerodynamic parameters, more control of element sizes and refinement.
Qualities	Higher design time, but more accurate results, lower average computational cost for the simulation itself.
Why Not Suitable?	Difficulty finding a converged solution for angles of attack other than zero.

3.3.3 - Final Mesh: Structured Parabolic C-Shape

After the problems experienced with the C-shape/rectangular mesh, by evaluating that the reason would be the discontinuity of the rectangular section, a natural step was to change the boundary shape of the enclosure. Thus, a parabolic C-shape geometry was designed and the mesh obtained, as can be seen in Figure 3.11.

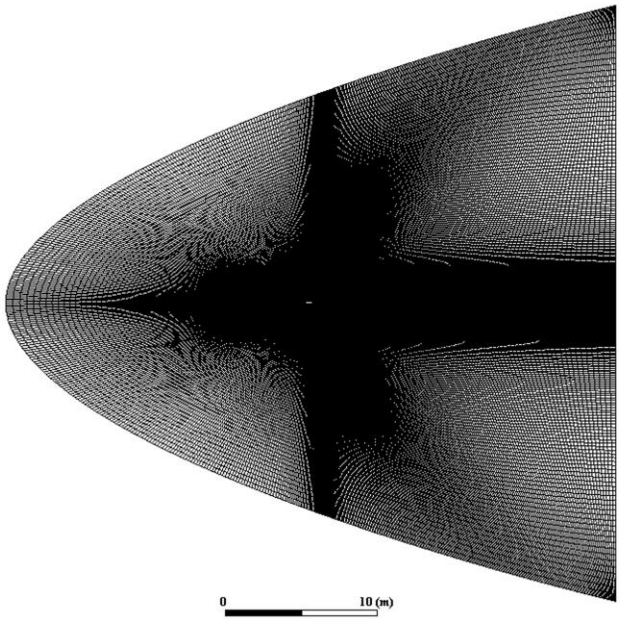

Figure 3.11 – Final mesh for both airfoil geometries.

The mesh shown in Figure 3.11 follow the same premises for the structured mesh explored in subsection 3.3.2. However, now there is no discontinuity in the boundary, thanks to the parabolic profile of the geometry, in a way that the flow can only follow one direction according to the boundary conditions imposed.

Furthermore, the new shape made the refinement more efficient, concentrating the high-density areas (of elements) only where it mattered the most: around the airfoil. This potentially reduced the simulation time and improved the precision of the results for the airfoil wall dynamics, while the number of elements decreased considerably. It is presented in Figure 3.12 detailed views of the final mesh around the standard airfoil configuration.

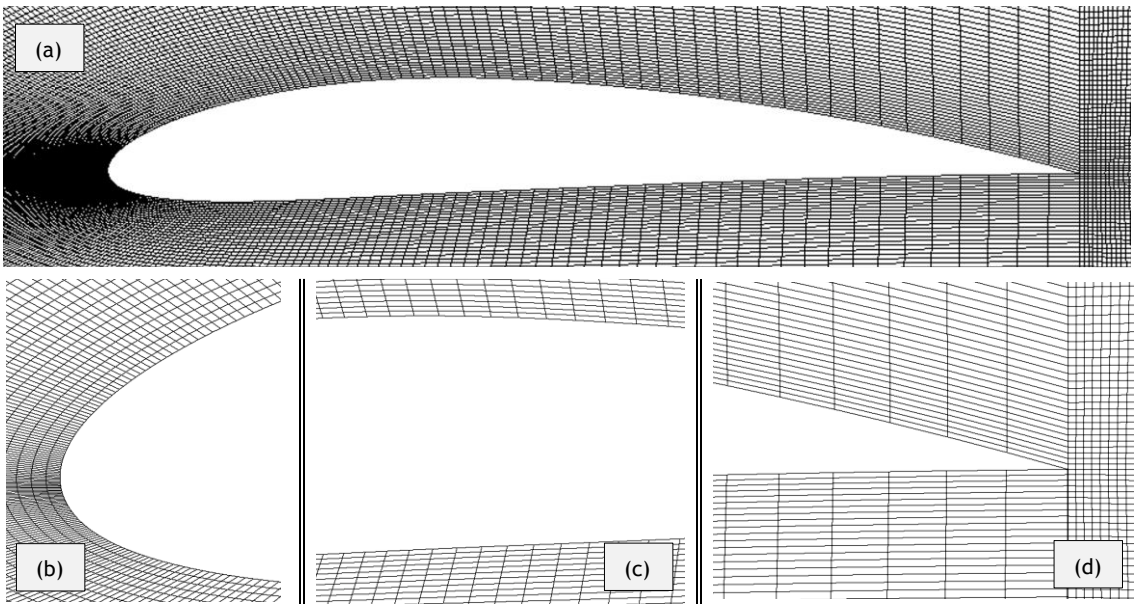

Figure 3.12 – Final mesh for standard airfoil geometry, detailed views of a) whole airfoil, b) leading edge, c) middle section and d) trailing edge.

In terms of mesh metrics, the mesh generated for the standard airfoil case had statistical parameters as presented in Table 3.7, considering the $640{,}200$ quadrilateral elements arranged on the model.

Table 3.7 – Mesh metrics for the structured parabolic C-shape grid, standard airfoil.

Parameter	Minimum	Maximum	Average
Skewness	1.1462×10^{-3}	0.54828	0.23944
Orthogonal Quality	0.65579	1	0.9154
Aspect Ratio	1.0002	120.04	4.9234

From Table 3.7, it is possible to notice that the lower level of general refinement reflected on the mesh metrics. Despite the rise in the average values, a much more equalized skewness was obtained, if compared to first structured mesh attempt. The same can be said for the orthogonal quality, while the aspect ratio improved considerably. Like stated before, these parameters only serve as references, as there is not a universal value or limit for them in order to assess mesh quality. However, this metrics indicates at least that the mesh was still in comparable (or even higher) quality to the previous one.

In Figure 3.13, it is shown the modified airfoil final mesh, with focus on the cavity implementation. It is only represented the first configuration and the position for case 1 and 3, as the remaining parts of the mesh was generated with the same settings from the standard case and the cavity itself maintained the same mesh when positioned upstream.

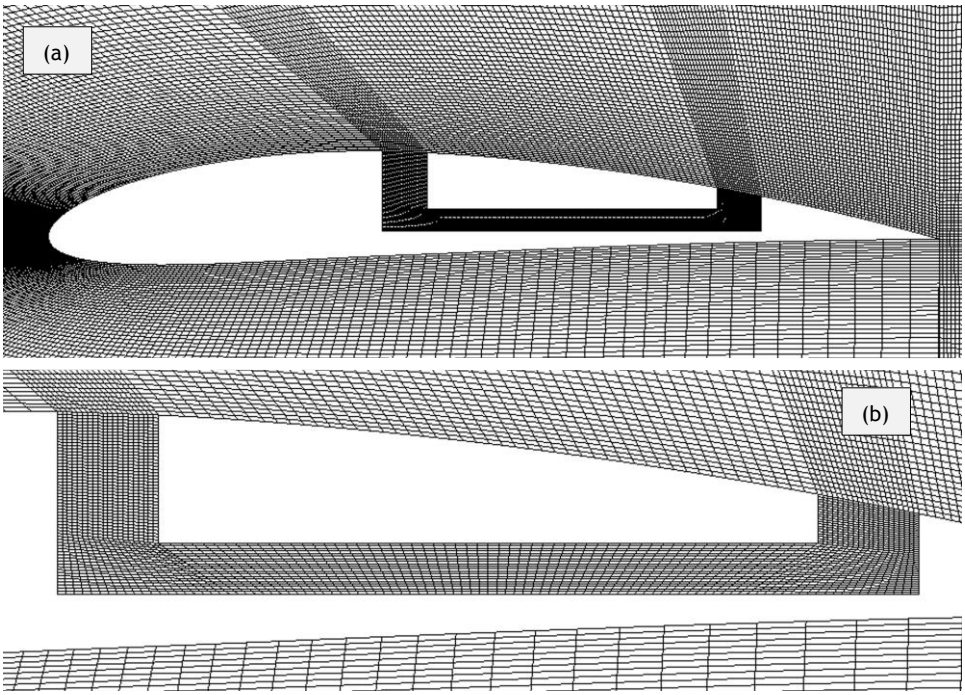

Figure 3.13 – Final mesh for modified airfoil geometry, detailed views of a) whole airfoil and b) first configuration of the cavity.

The statistical parameters for the modified case are presented in Table 3.8. These values are for reference and comparison only and are only valid for the cases represented by Figure 3.13, as the slightest change in the geometry varies these parameters. However, all meshes used in the modified airfoil study (28 meshes) had metrics considered excellent (or good, at least) within the CFD good practices[3] guideline, regarding the $671{,}400$ quadrilateral elements.

Table 3.8 – Mesh metrics for the structured parabolic C-shape grid, modified airfoil.

Parameter	Minimum	Maximum	Average
Skewness	1.112×10^{-3}	0.66859	0.24949
Orthogonal Quality	0.50387	1	0.90627
Aspect Ratio	1.0004	120.04	5.0126

[3] For example, the literature considers grids with average skewness values between $0.5 - 0.75$ a fair quality mesh, while between $0.25 - 0.5$ a good mesh. Below those values the mesh could be considered excellent [32].

Finally, it is important to notice that the y^+ values for all cases simulated in the present work with the final mesh were kept within a safe range (really small values or $30 < y^+ < 300$) to ensure good results [33]. This measure was taken more as a precaution, as the turbulence model used – Spalart-Almaras [20] – is sufficient robust to deal with any y^+ size (due to an enhanced wall-treatment implementation).

3.4 - Boundary Conditions

After quality meshes were obtained, the last step before the CFD simulation itself was the determination and imposition of boundary conditions on the model. Although there was an unlimited combination of settings that could produce good and consistent results, keeping the method and project objectives in mind was very important, in order to achieve relevant meaning for the solutions.

The approach taken in the present work to determine the boundary conditions was to make the simulations as close as possible to experimental conditions available in the literature. Thus, the environmental parameters used were the same from the wind tunnel experiments described on the NACA report about compressible effect on the NACA 4412 airfoil [34], together with a chosen validation angle of attack and Mach number. This made possible the comparisons between a standard airfoil simulation and the experimental data, validating the results and giving support to the unique simulations of the cavity cases that would follow. Therefore, the environmental parameters were kept constant in all simulations performed in the current work.

The Table 3.9 presents the air environmental conditions imposed on the boundaries, where the flow could be considered as having freestream properties.

Table 3.9 – Environmental conditions of air used in all simulations.

Parameter	Value [unit]
Temperature (T_∞)	$288.15\ [K]$ or $15\ [°C]$
Absolute Pressure (P_∞)	$101{,}325\ [Pa]$
Reference Density	$1.2255\ [kg/m^3]$

In terms of material properties (air), some assumptions had to be made and configured in the solver to ensure a good convergence and results. As all the boundaries were defined as *pressure-far-field* and the flow was essentially compressible, air density was set to be governed by the ideal gas law. The air viscosity was assumed as function of temperature using Sutherland's viscosity law in the three-coefficient mode [35], defined by equation (3.1).

$$\mu = \mu_0 \left(\frac{T}{T_0}\right)^{\frac{3}{2}} \frac{\mathrm{T}_0 + \mathrm{S}}{T + S} \tag{3.1}$$

Where μ is the dynamic viscosity in $kg/m.s$, T is the static temperature of the fluid in K, μ_0 is a reference viscosity value in $kg/m.s$, T_0 is a reference temperature value in K and S is the Sutherland constant also in K, an effective temperature value that is characteristic of the gas.

For the implementation and considering that the flow would stay at moderate temperatures given the freestream conditions, the three constants were assumed as their default values: $\mu_0 = 1.716 \times 10^{-5}\ kg/m.s$, $T_0 = 273.11\ K$ and $S = 110.56\ K$ [35].

It is important to notice that both ideal gas law and Sutherland's viscosity law were already implemented and were part of the solver provided by the ANSYS® Fluent® environment.

Finally, the last configuration in terms of boundary conditions was to set the angles of attack (α) and the Mach Number of the flow. The Mach number of 0.717 was chosen according to the experimental data from the referred NACA report [34] and it was so that a transonic flow and the effect of the shock could be evaluated in the best way possible, considering the results from the wind tunnel tests available.

For the AoAs, the validation angle of $-0° 15'$ was aligned to one of the experiments available in the literature [34], while the standard airfoil tests were performed following a general range of angles based on missions, starting in $0°$ all the way to $14°$, in increments of $2°$. This allowed to evaluate the effects of separation on the standard airfoil geometry, and to choose the best scenario to run the modified airfoil cases, as will be discussed in Chapter 4. All the 28 modified airfoil cases were run under the same angle of attack.

The Table 3.10 shows the angles of attack and the Mach number considered according to each case.

Table 3.10 – Angles of attack and Mach number used in all simulations.

Simulation	AoA (α)	Mach Number (M_∞)
Validation	$-0° 15'$	0.717
Standard Airfoil	$0°: 2°: 14°$	
Modified Airfoil	$2°$	

After the boundary conditions were established, all cases were simulated using the Spalart-Allmaras turbulence model (as stated before in section 2.3), considering a pressure-based solver and a steady state assumption. This is because this type of turbulent flow, scope of the present work, usually tends to a stationary state where the fluid properties are time-independent. The simulations were run for a sufficient amount of iterations until the residuals

and the aerodynamic coefficients (lift and drag) were statistically converged, or in other words, remained invariant. All tests were performed in a computer cluster, as stated before, and had run times of 5 hours, approximately. The results and relevant analyses will be presented in Chapter 4.

In Figure 3.14, it is possible to see a diagram summarizing the main boundary conditions imposed to the simulations.

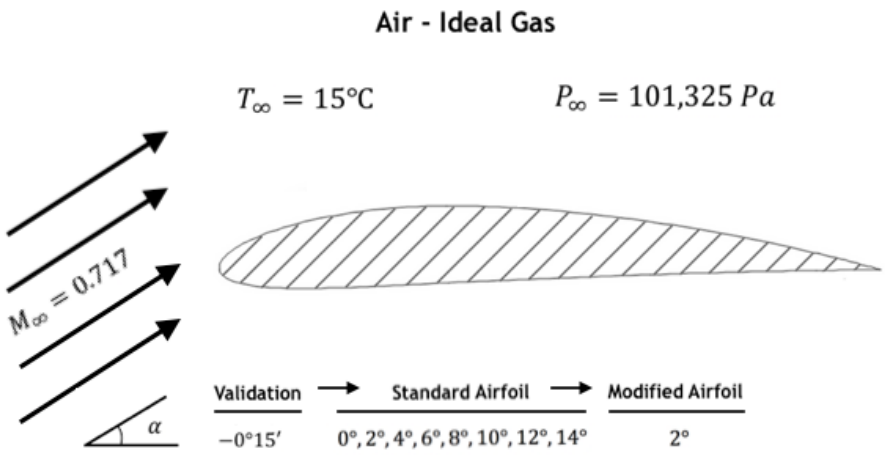

Figure 3.14 – Main boundary conditions used in all simulations.

3.5 - Conclusion

The methodology of the present work discussed in this chapter represents the base of the project, from which the results were obtained. Without a good methodology, any engineering or scientific work loses relevance and meaning. That is why this chapter tried to present the most important aspects and nuances of the simulations performed.

First, a basic outline was presented in order to show how the project was structured and how the workflow was defined, followed by a discussion about the geometries. Throughout the present work, two types of geometries were used, a standard airfoil profile of the NACA 4412 and modified ones, where the cavity cases were implemented.

After covering the main aspects and parameters of the geometries, three mesh attempts were presented, being the last one the final mesh used in all simulations. The final mesh brought a modification from the previous attempt, with the introduction of a parabolic boundary that ensured good convergence for all angles of attack tested. Being a structured grid, the metrics for both standard and modified airfoil cases reflected a good (or even excellent) mesh quality according to the literature, allowing the project to proceed. Quality that would be reassured after the validation test.

Lastly, the boundary conditions were discussed, and the final parameters required to run the simulations were presented. Most of the boundary conditions imposed were aligned to the

ones used in wind tunnel experiments performed by the NACA itself [34]. That way, not only comparisons between the standard profile and experimental data could be made, but it also would give the modified cases a wind tunnel scenario that could eventually approximate the simulations of this project to experiments performed in the context of a future work.

Chapter 4

Results and Analyses

The previous chapters discussed many aspects of the present work, from the motivation and objectives, passing through a brief theoretical review and reaching the project methodology, covering essential settings and assumptions considered in the implementations.

This chapter now presents the results obtained in all simulations and the relevant analyses. First, the validation test will be explored in full, leading to the standard airfoil cases discussion. Afterwards, the modified airfoil results will be presented, case by case, where each one will be analysed individually.

Finally, the cases will be compared in terms of lift and drag coefficients, allowing to determinate which one had the best performance and evaluate potential improvements on the model.

4.1 - Validation Test

As stated before, the first step performed in the context of the present work was to validate the assumptions and hypotheses adopted during the design phase. Of course, several preliminary tests were run before the validation test itself could be implemented, however, being able to obtain results close to experimental data available in the literature would represent the initial step towards the main objectives of the project, certifying that the next simulations would be as close as possible to the real dynamics of the flow.

After analysing the reports and the experimental data available on the airfoil NACA 4412 [34], a wind tunnel test at Mach number 0.717 and $-0°15'$ angle of attack was chosen to be implemented in the CFD simulation and serve as case comparison, as the most important phenomena could be seen in the referred experiment.

In Figure 4.1, it is possible to see the results of the validation test in terms of pressure coefficient and Mach number.

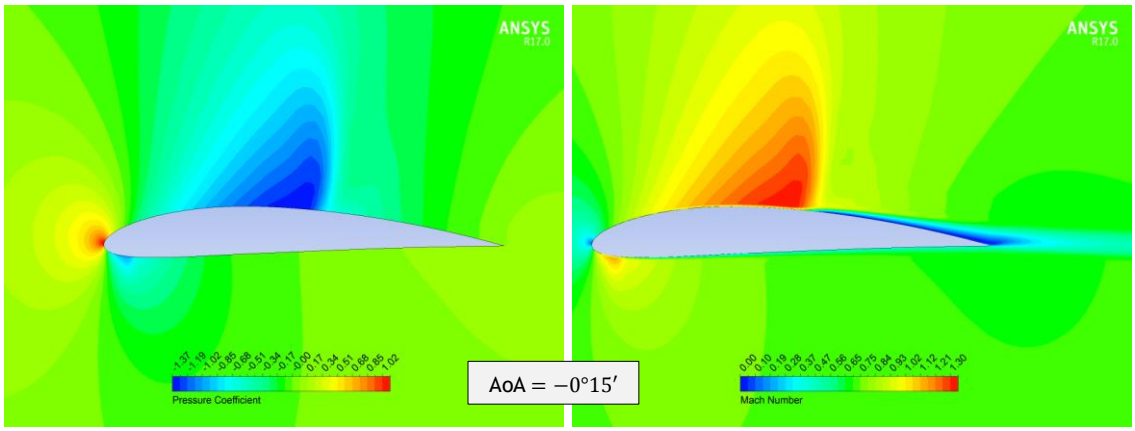

Figure 4.1 – Pressure coefficient and Mach number contours for the validation test.

In Figure 4.1, the main phenomena occurring in a transonic flow over an airfoil is represented. It is possible to observe the shock region in both contours, where the fluid properties change abruptly. After the shock, the pressure increases almost instantly, while the Mach number decreases to a subsonic state. A small flow detachment is observed after the shock as well, which is not so expressive due to the low angle of attack.

A good way to compare the simulated results to the experimental data available in the literature [34] was to evaluate the pressure distribution around the airfoil. The graph shown in Figure 4.2 brings the simulated (solid line) and experimental (triangle symbol and dash-dot line) pressure distribution for the NACA 4412 airfoil.

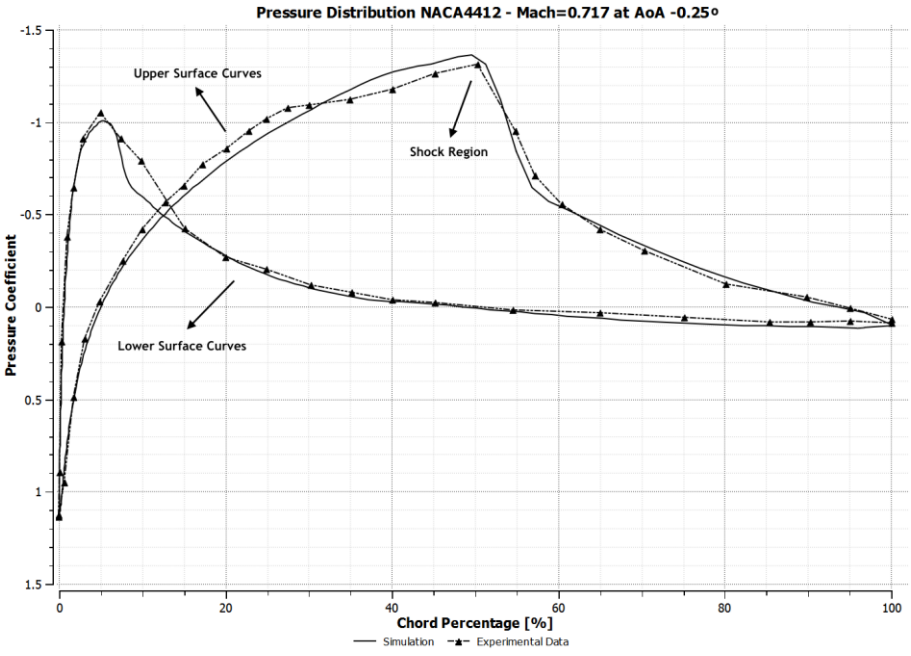

Figure 4.2 – Experimental and simulated pressure distribution for NACA 4412 airfoil, pressure coefficient (inverted axis) *versus* chord percentage.

From Figure 4.2, it is possible to see that the simulated data obtained are close to the wind tunnel test available in the literature, at Mach 0.717 and AoA $-0°15'$ (or in decimal

notation $-0.25°$). However, some small differences appear, especially near the shock region, due to simplification assumptions adopted in the implementation process and in the turbulence model itself. Also, it is not possible to neglect potential imprecisions of the experiment, but as seen in Figure 4.2, the validation can be considered satisfactory for the purposes of the present work, with main features such as shock location preserved in the simulation. This enabled the project to continue using the model and the initial assumptions in the simulations to come.

The shock location and the pressure differences shown in Figure 4.1 and especially in Figure 4.2 are the core features that make the secondary flow possible, with the passive suction leading to a potential flow reattachment and drag reduction, as will be explored in the next sections.

4.2 - Standard Airfoil Simulations

After the validation test enabled the model and the initial assumptions, the next step was to implement the standard airfoil simulations. In Figure 4.3, it is presented the results for $0°$ and $2°$ in terms of pressure coefficient and Mach number.

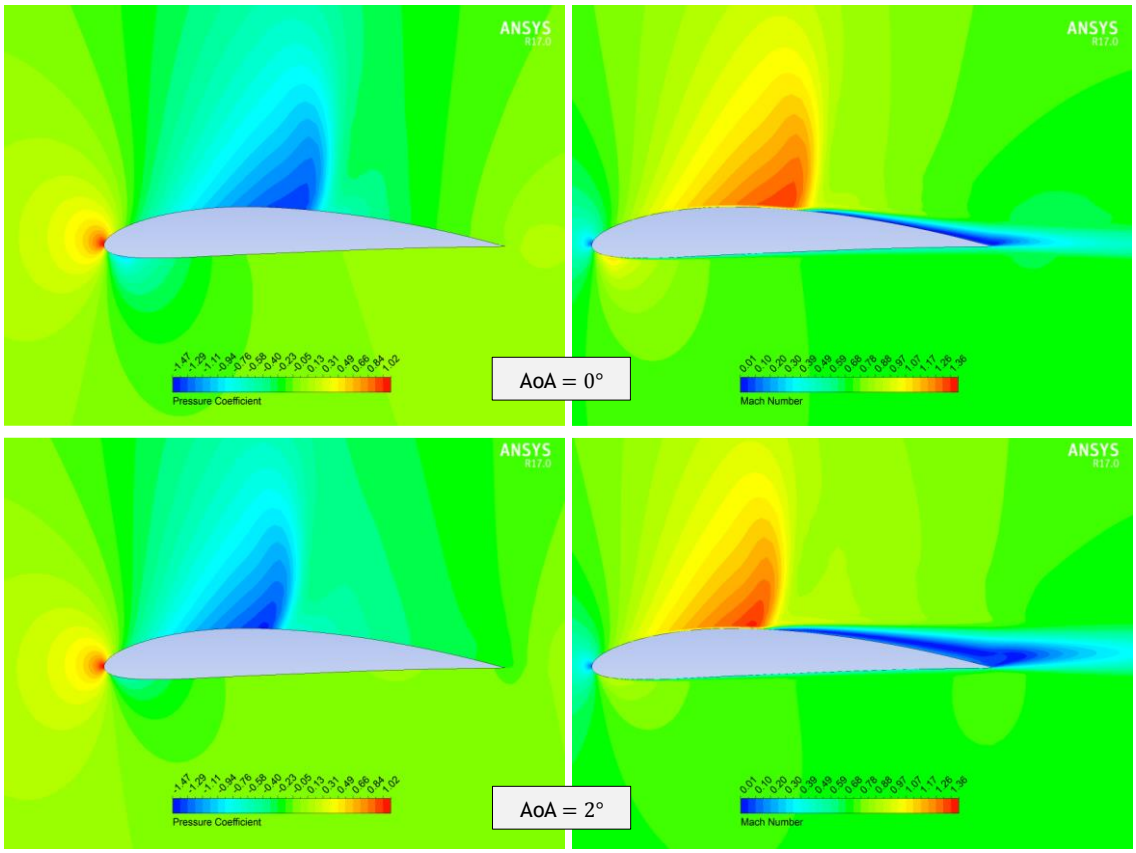

Figure 4.3 – Pressure coefficient and Mach number contours for the standard airfoil simulations: $0°$ and $2°$ of angle of attack.

The standard airfoil simulations were defined at several angles of attack (keeping the same Mach number from the validation), in order to evaluate the flow separation and choose the most suitable case for the modified simulations. In Figure 4.4, it is shown the results for 4°, 6° and 8° of angle of attack.

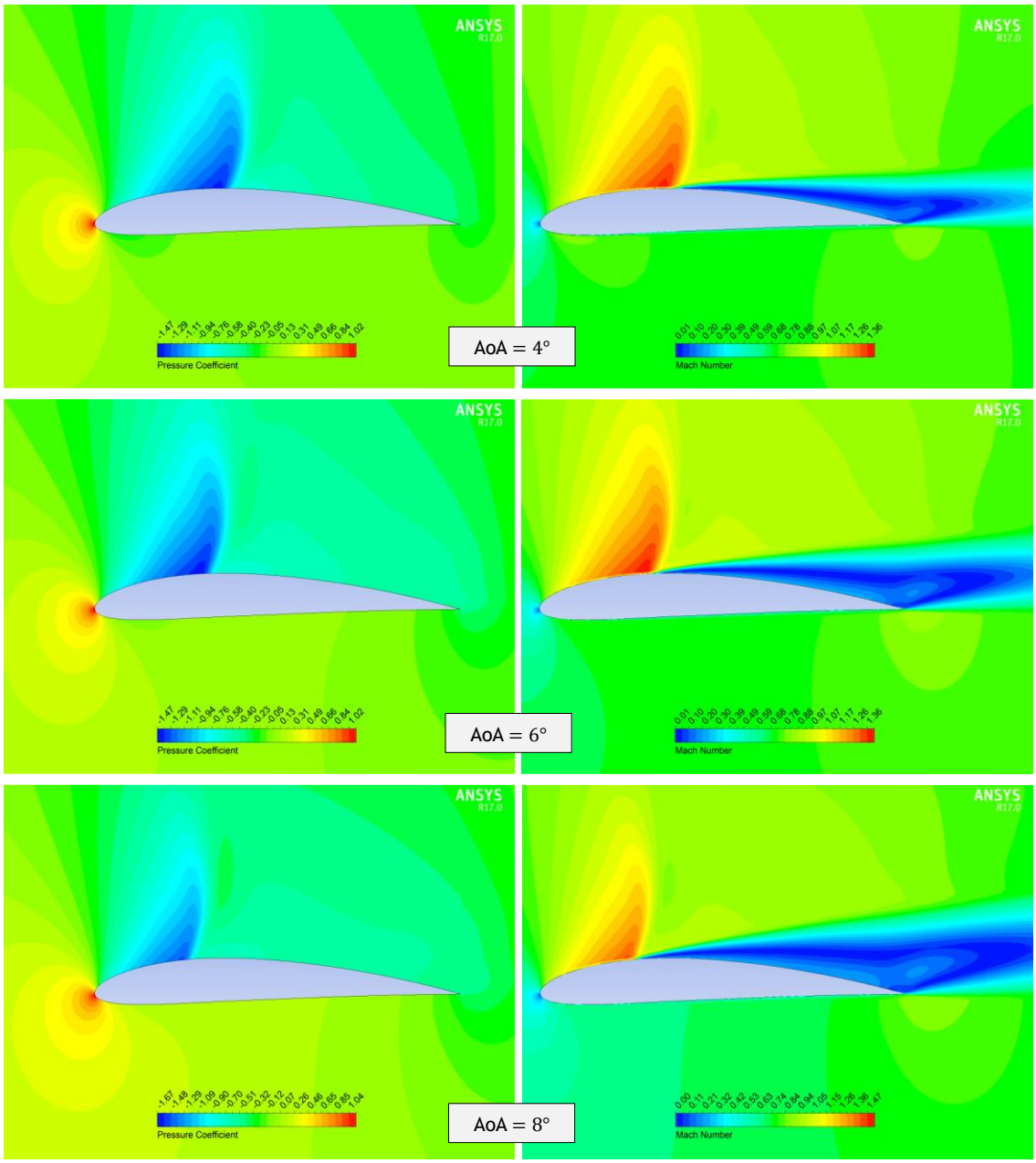

Figure 4.4 – Pressure coefficient and Mach number contours for the standard airfoil simulations: 4°, 6° and 8° of angle of attack.

In Figure 4.3 and Figure 4.4, it is possible to notice certain flow particularities that is obtained once the angle of attack is varied. First, the shock location is moving upstream as expected and becoming weaker as the pressure gradient reduces due to the airfoil geometry. Second, the flow separation is increasingly becoming more evident and happening more upstream, resulted from the shock location variation and the higher angles of attack. The

same phenomena can be seen in Figure 4.5, when the angle of attack was increased even more.

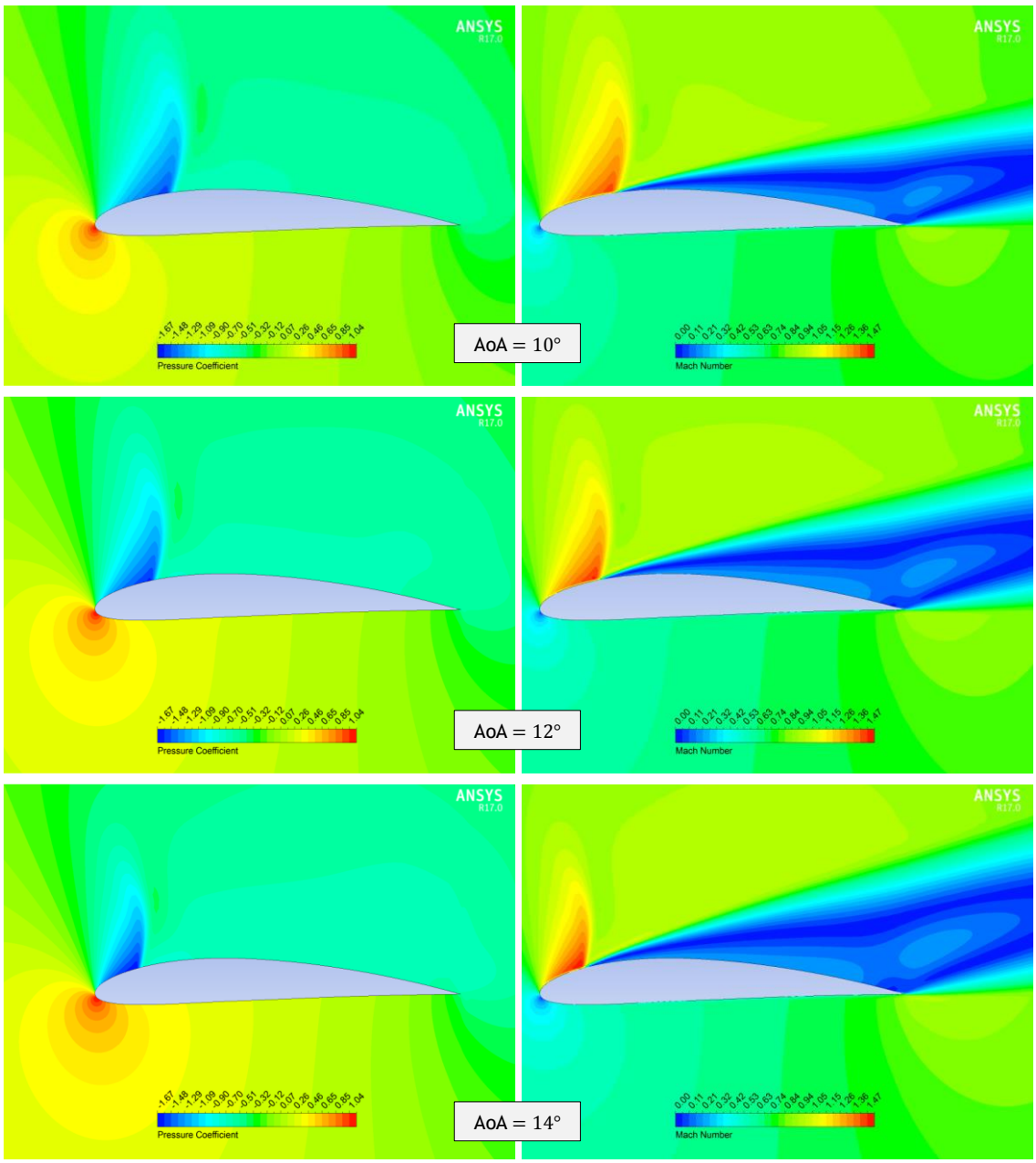

Figure 4.5 – Pressure coefficient and Mach number contours for the standard airfoil simulations: 10°, 12° and 14° of angle of attack.

From Figure 4.5, it is important to observe how the flow is almost totally separated. Of course, the simulations could continue up to the point of critical angle of attack (where stall occurs), or even more to show how the effect of separation reduces the lift, but this would not be within the scope of the present work.

Considering the results shown in Figure 4.3, Figure 4.4 and Figure 4.5 and the standard operation angle of attacks during cruise [36], 2° was chosen as the angle of attack for the modified airfoil cases implementation. It is known that the angle of attack changes during all

phases of flight, and even during cruise as the weight reduces with fuel consumption. However, many airliners have $2°$ as standard operation angle [36], and exploring the angle in which the aircraft stays for as long as possible during the mission would bring more benefits in the event of drag reduction, potentially leading to more fuel saving.

It is important to notice that other angles could be tested to approximate the theory to a specific aircraft model, for example, or even to adapt the simulation to other types of missions. However, considering the academic nature of the present work and as proof of concept, staying as general as possible could only bring advantages to future works in the subject.

In this context, Figure 4.6 presents the pressure distribution around the airfoil at $2°$ of angle of attack.

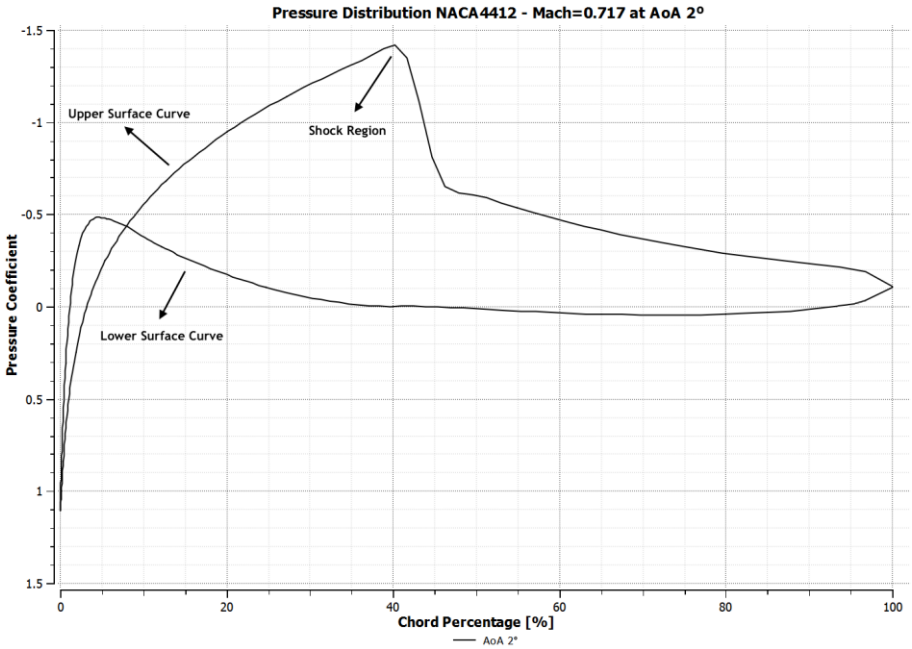

Figure 4.6 – Pressure distribution for NACA 4412 airfoil at $2°$, pressure coefficient (inverted axis) *versus* chord percentage.

The Figure 4.6 brings an important parameter to the implementation of the modified airfoil geometry, main subject of the present work. From the graph, it is possible to define the shock location, that occurs approximately around 40% of the airfoil chord. The two cavity positions considered in the four cases of the modified airfoil simulations (section 3.2) were placed in regions that would present a high pressure gradient, but still followed the project premises of 1) having a cavity encompassing the area where the shock occurred and 2) testing another position with the shock in the middle.

Lastly, it is important to notice that the results obtained for the standard airfoil simulation at $2°$ of angle of attack were used as baseline for the modified airfoil simulations, presented in sections 4.3 and 4.4.

4.3 - Modified Airfoil Simulations

After the contours and pressure distributions for the standard airfoil simulations were determined, the next subsections will present the results in terms of Mach number for each case of the modified airfoil simulations separately, according to the schematics shown in Figure 3.5 and Figure 3.6.

The results were organized by semi-cavity length, being the left number on the label the upstream semi-cavity length, and the right number, the downstream semi-cavity length. It is also displayed a detailed view of the cavity with vectors showing the secondary flow. The Mach number was chosen as working variable to allow the flow separation and the secondary flow dynamics inside the cavity evaluation.

4.3.1 - Case 1

In Figure 4.7, it is shown the Mach number contour and a detailed view for case 1, cavity lengths 50 and $75\ mm$.

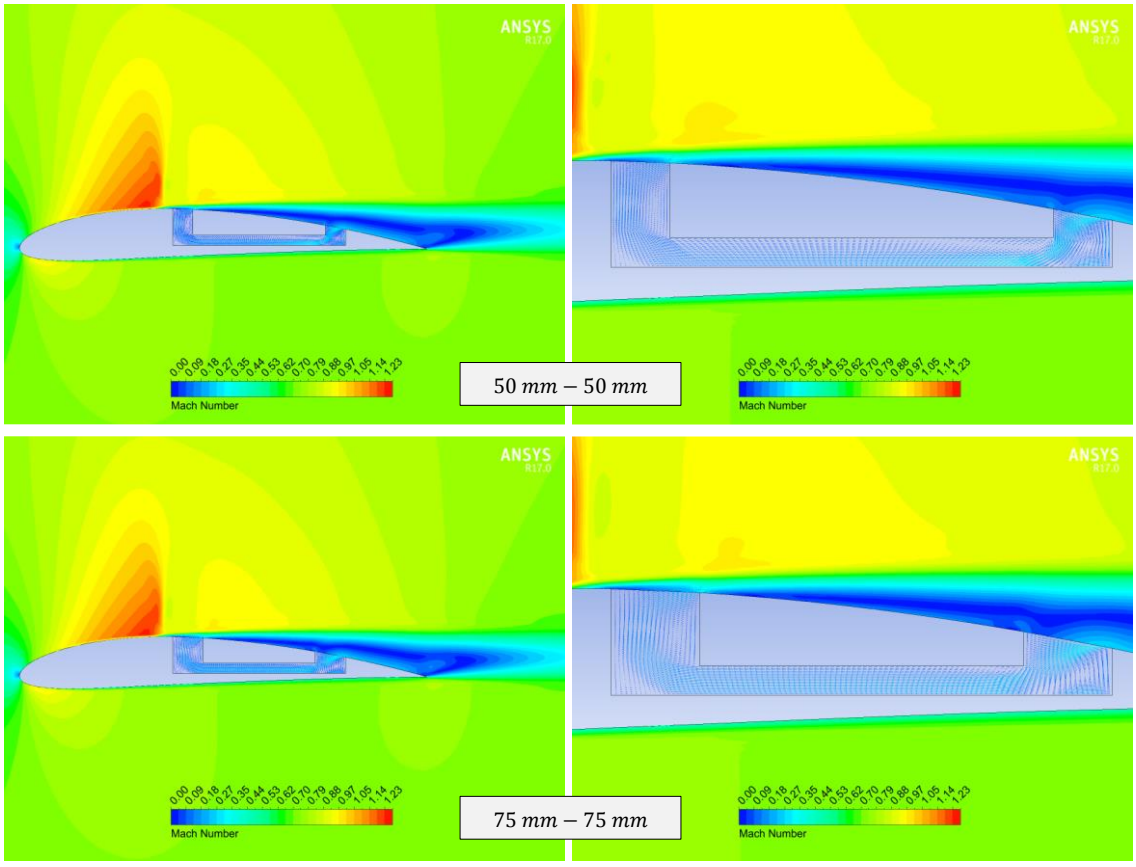

Figure 4.7 – Mach number contour and detailed view, case 1, cavity lengths 50 and $75\ mm$.

In the first set of results displayed in Figure 4.7, it is possible to see right way that the cavity moved the shock location more upstream if compared to the baseline standard airfoil, albeit it was still present and relevant to the flow dynamics. With the secondary flow,

it is evident that the flow separation was retarded, and the passive suction started to interfere with the boundary layer height.

In Figure 4.8, these same effects can be observed for cavity lengths of 100, 125 and $150\ mm$.

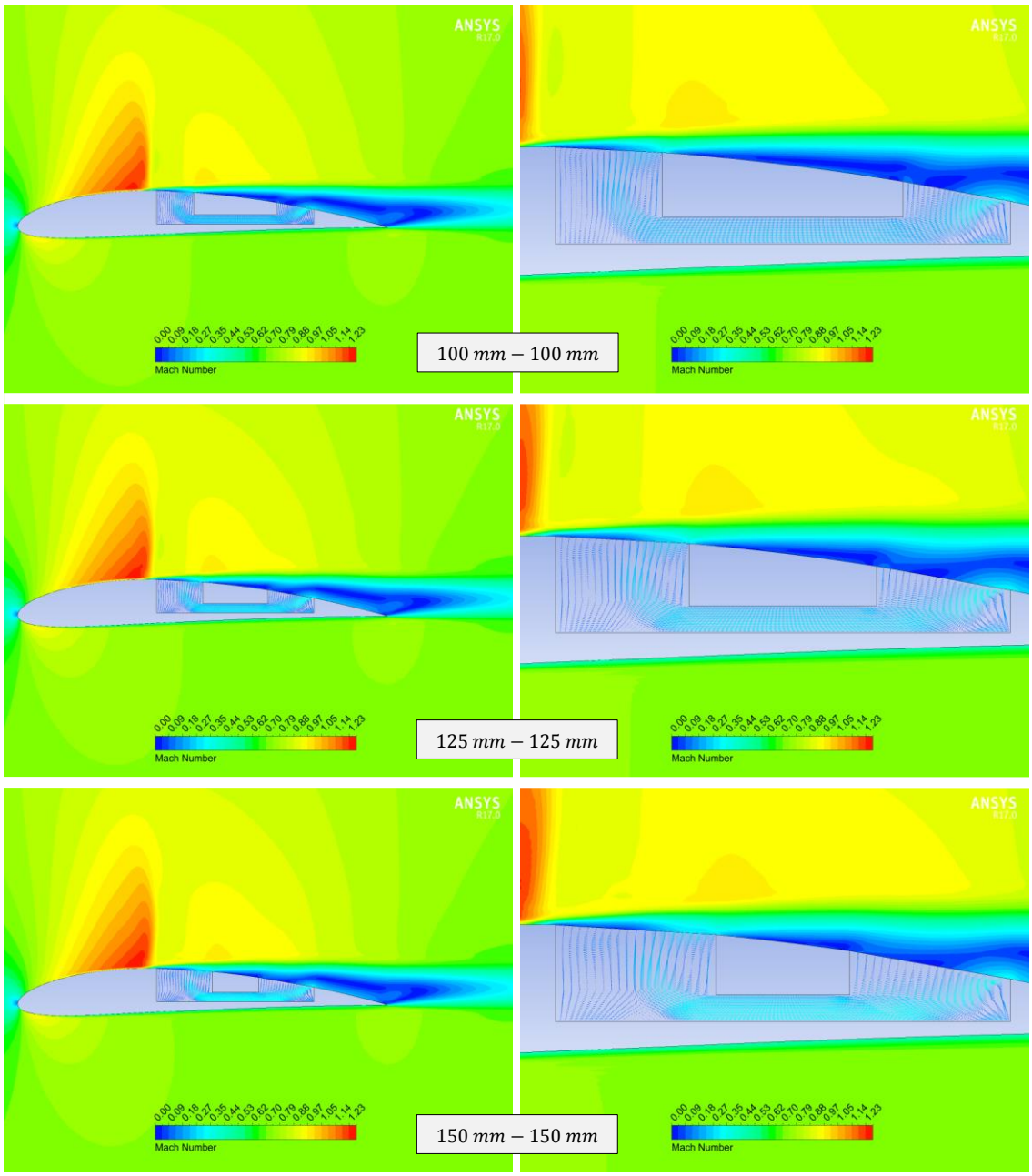

Figure 4.8 – Mach number contour and detailed view, case 1, cavity lengths 100, 125 and $150\ mm$.

As the cavity lengths increased, the passive suction was more and more evident, as can be seen in Figure 4.8. Due to the cavity size, some small recirculation zones appeared, which was represented by the vectors in the detailed views. These recirculation occurrences were expected considering the velocity difference between the main flow and the flow inside the cavity.

Figure 4.9 brings the last set of results for case 1, showing the contours for the cavity lengths of 175 and $200\ mm$.

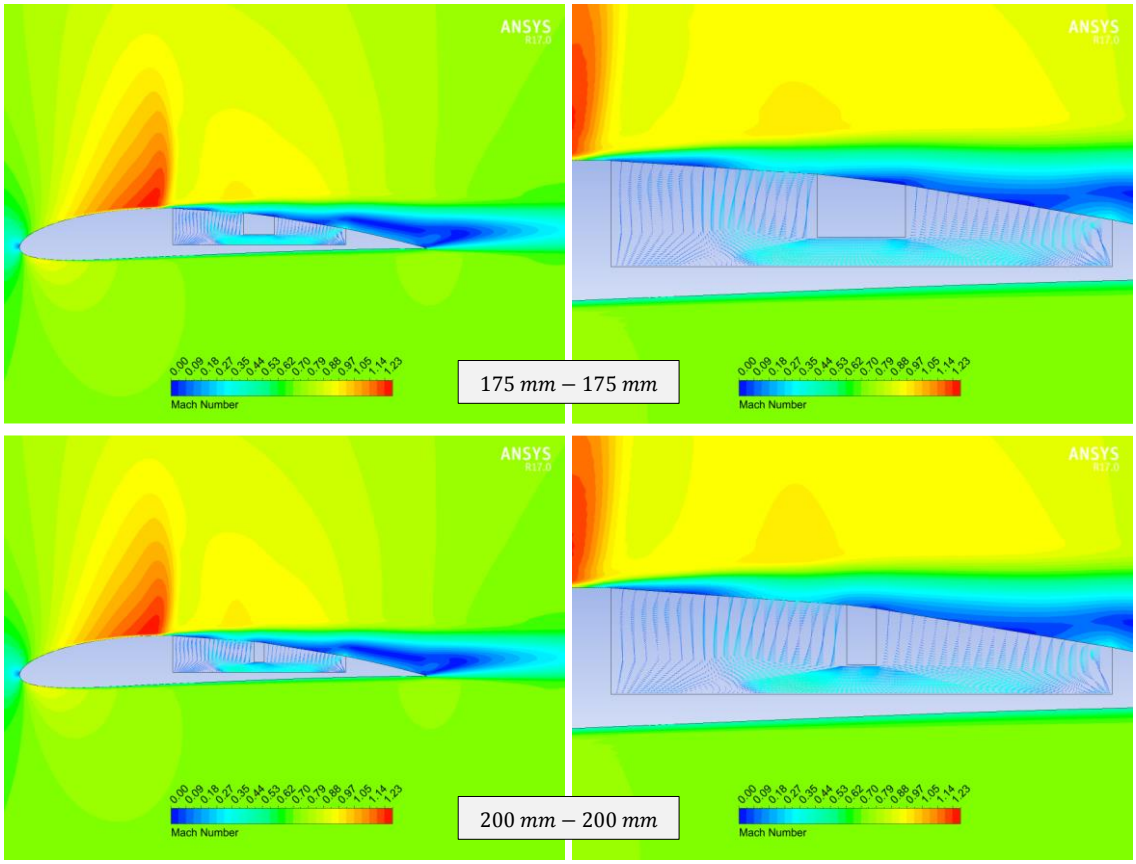

Figure 4.9 – Mach number contour and detailed view, case 1, cavity lengths 175 and $200\ mm$.

In Figure 4.9, it is possible to see that the secondary flow affected even more the boundary layer, although creating some turbulent, recirculation zones inside and near the cavity entrance/exit. These "dead zones" of the secondary flow is expected to potentially impact the drag and lift coefficients, as will be explored in section 4.4.

4.3.2 - Case 2

In case 2 simulations, the cavity position was changed upstream but the same length increments from case 1 was kept. As stated before, the main idea was to test what effect the cavity would produce considering the original shock position in the middle of both semi-cavities. The semi-cavities location was defined according to the pressure distribution shown in Figure 4.6.

In Figure 4.10, it is presented the results for 50 and $100\ mm$, in the new position upstream.

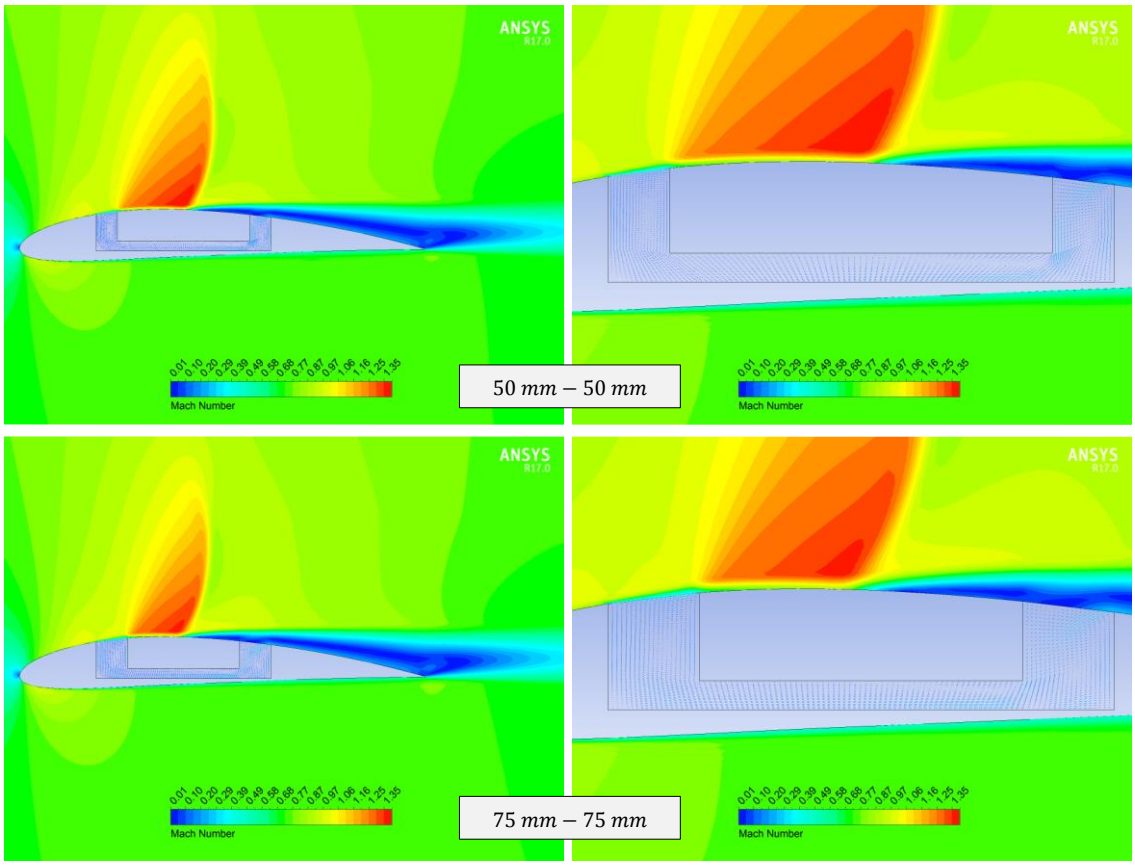

Figure 4.10 – Mach number contour and detailed view, case 2, cavity lengths 50 and $75\ mm$.

Considering the contours displayed in Figure 4.10, it is possible to observe some interesting effects that differ from case 1. First, the shock position was kept the same as the original simulation for the standard airfoil, however, its extension was limited upstream by the first semi-cavity. This potentially could lead to a shock-induced drag reduction, although its contribution in the total drag is not the most relevant. Second, the flow separation occurred in the same point as the original simulation, which could counterbalance the potential shock reduction influence.

Another important aspect to notice is that these first two lengths did not produce a relevant suction effect in the boundary layer. Just like in case 1, this was expected considering the limited mass flow rate of these first two configurations.

These described effects can be seen much more pronounced in Figure 4.11, where it is presented the simulations for cavity lengths of 100, 125 and $150\ mm$.

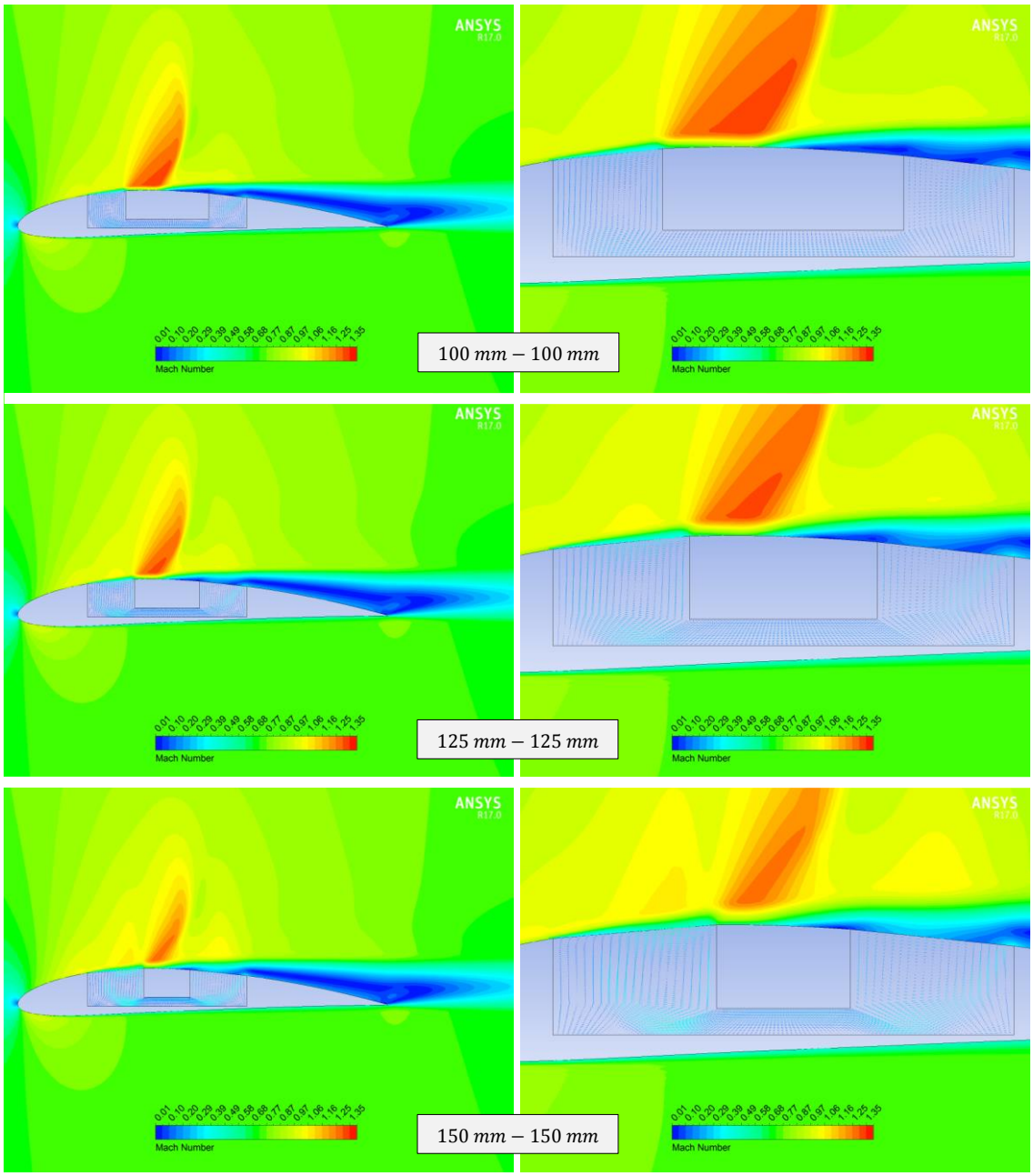

Figure 4.11 – Mach number contour and detailed view, case 2, cavity lengths 100, 125 and $150\ mm$.

Continuing the case 2 analysis, the lengths 100, 125 and $150\ mm$ presented in Figure 4.11 caused a much more impact in the main flow. The shock was totally weakened and even though the separation started in the same original point, the suction effect caused a partial reattachment. This however would not necessarily result in drag reduction, as this effect was just more pronounced in the bigger cavities. It is also important to notice that some of the flow near the cavity entrance (downstream semi-cavity) was reversed, which could impact negatively in getting better aerodynamic coefficients.

Incrementing even more the cavity towards the centre, the final two configurations with lengths 175 and $200\ mm$ are presented in Figure 4.12.

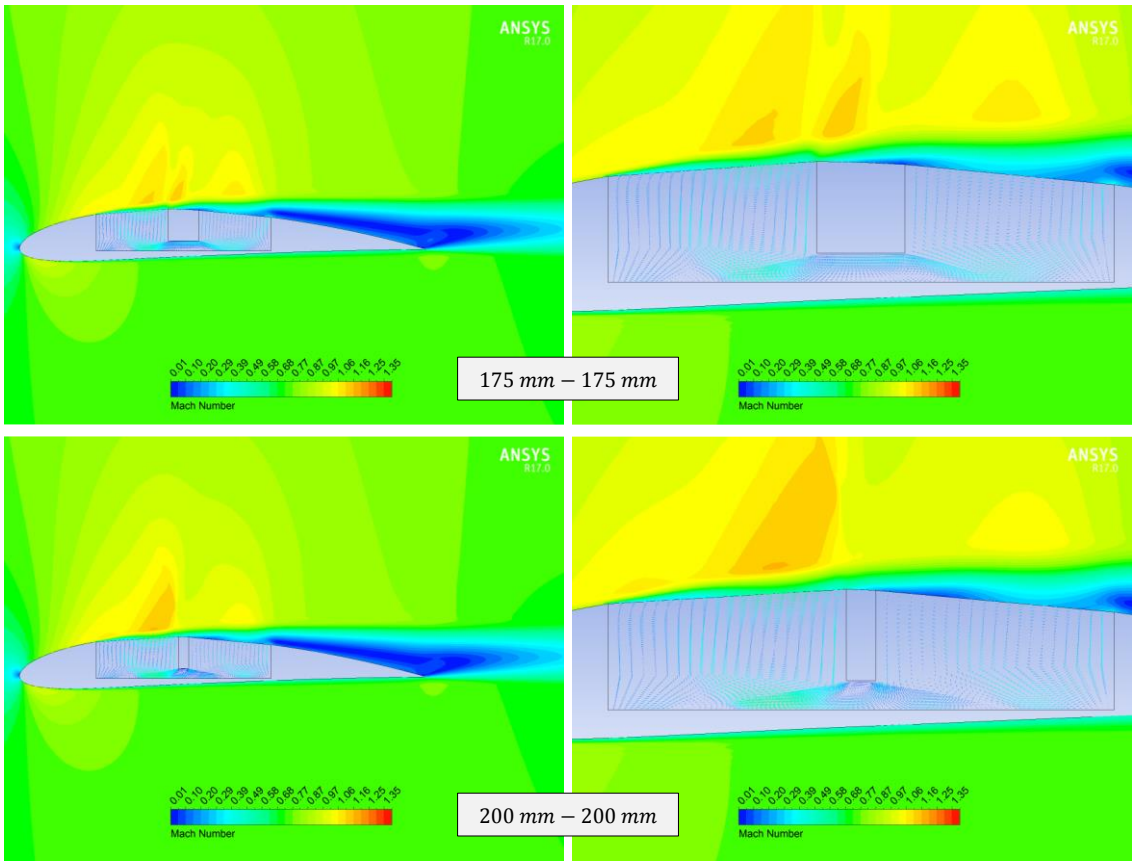

Figure 4.12 – Mach number contour and detailed view, case 2, cavity lengths 175 and 200 mm.

Lastly, in Figure 4.12, it was observed almost a total shock disappearance, with the same effects obtained in the bigger cavities from case 1, such as “dead zones”, turbulence and recirculation areas in the secondary flow. The fact that the shock was nearly extinguished by the cavities could have certain applications depending on missions, so this was an important characteristic to notice in case 2, although a cavity configuration so upstream wouldn’t help in terms of the drag reduction and/or lift increase, as will be discussed in section 4.4.

4.3.3 - Case 3

After the first two cases, a different approach was taken in case 3 and 4, where the semi-cavity upstream was kept at a fixed length in order to regulate the suction effect. In case 3, however, the position adopted was the same from case 1, considering the original shock location just above the upstream semi-cavity.

As the length was fixed in 50 mm for the first semi-cavity, the Figure 4.13 brings the results for lengths of 50, 100 and 150 mm. Notice that the 50 mm configuration is identical to the first one presented in the case 1 results (Figure 4.7) but was included here for consistency purposes.

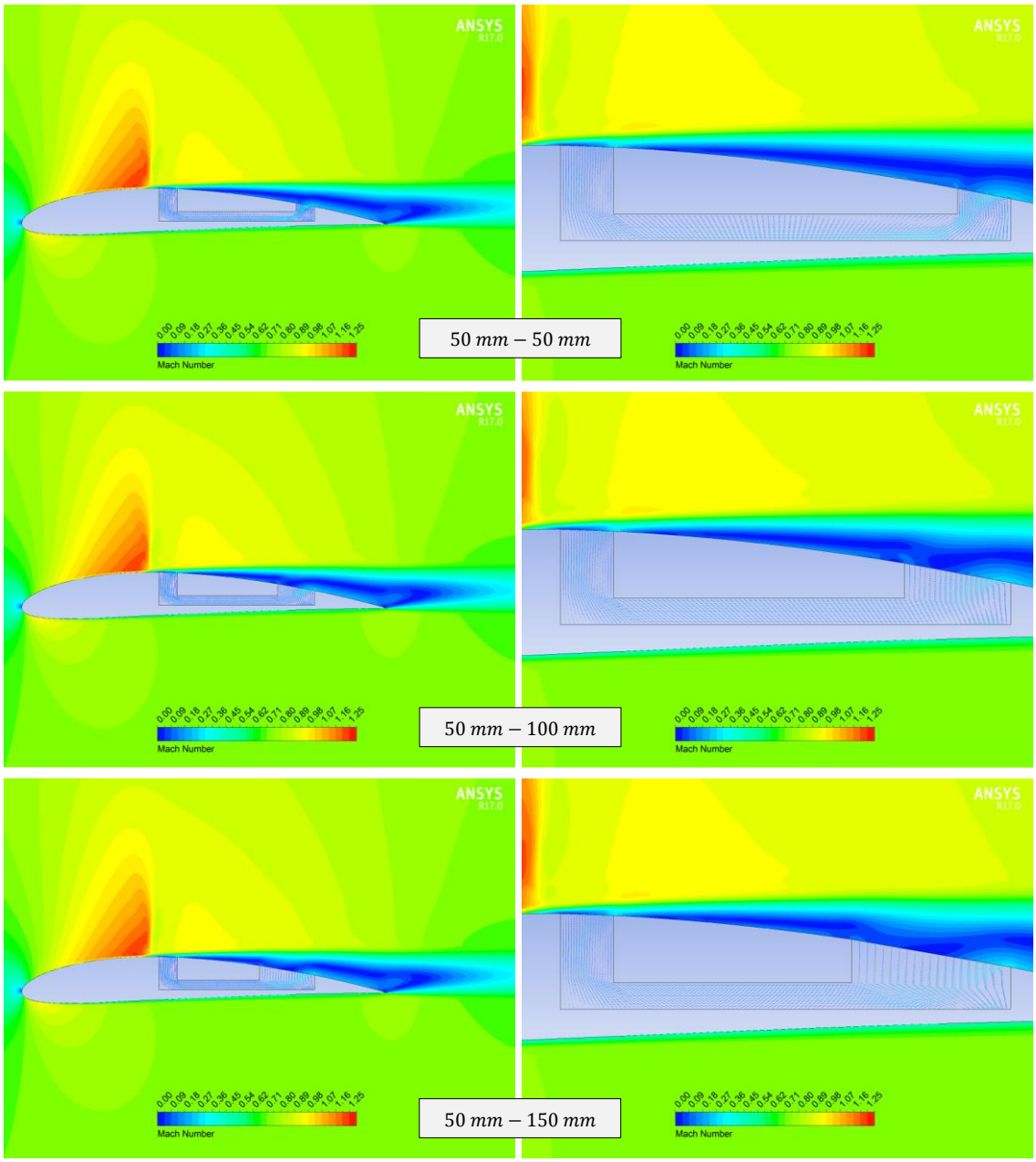

Figure 4.13 – Mach number contour and detailed view, case 3, cavity lengths 50, 100 and $150\ mm$.

In Figure 4.13, the same effect of case 1 appeared regarding the shock. The shock moved more upstream and the separation began to happen just after the first semi-cavity. In the 100 and $150\ mm$ configuration, the impact in the boundary layer height was noticeable, despite the fact of not being so prominent yet.

Due to the moderate size of the downstream semi-cavity shown in Figure 4.13, the secondary flow was still following the channel course, so recirculation areas were not too evident, as can be seen by the vectors' representation. These effects were quite stronger in the next increments, brought by Figure 4.14.

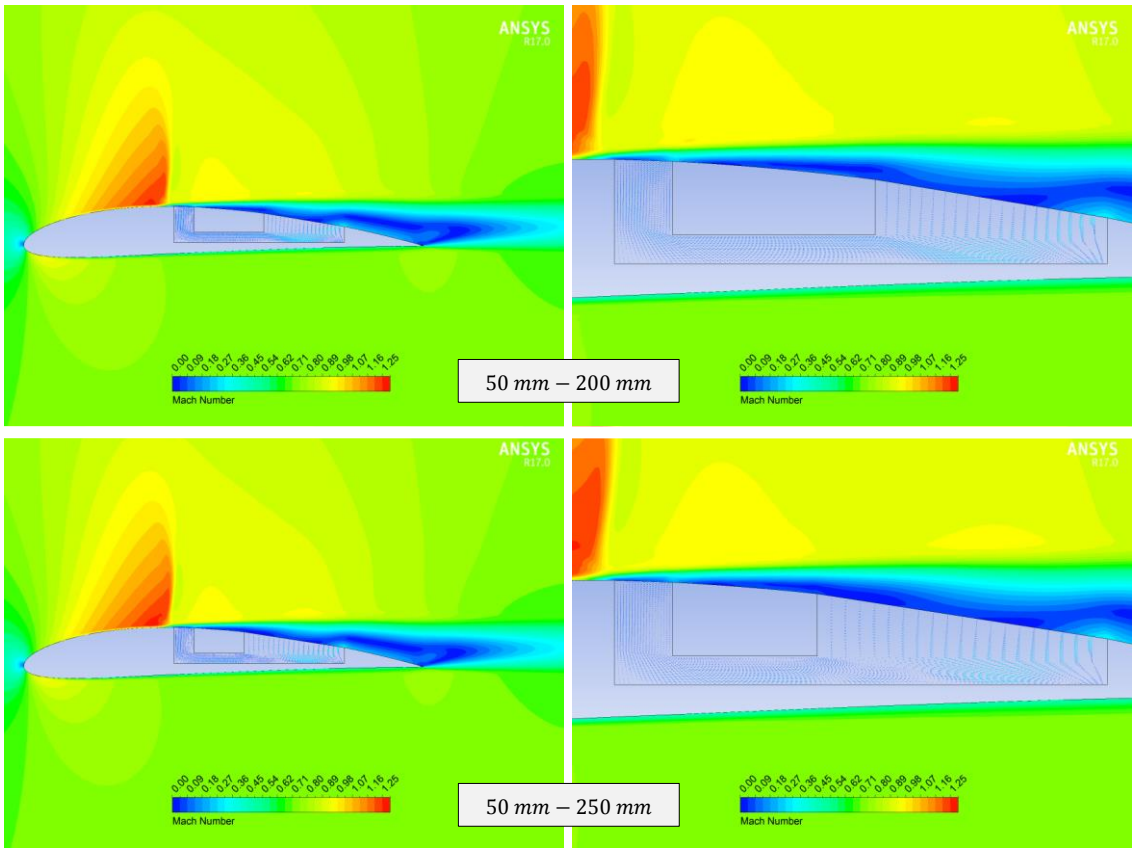

Figure 4.14 – Mach number contour and detailed view, case 3, cavity lengths 200 and $250\ mm$.

From Figure 4.14, it is possible to see that the suction became much stronger in the configurations of 200 and $250\ mm$, and was affecting the boundary layer and the flow separation. The fixed length upstream created a small bump area in the main flow due to the discharge velocity, although it is expected that the influence of such characteristic would not be too relevant in the aerodynamic coefficients.

The bigger cavity size downstream of the $250\ mm$ length created that recirculation and "dead zones" again, which, although expected, cannot be considered beneficial in terms of drag reduction either. In addition, the increase in size produced an even stronger reversed flow which is evident from the vectors in the detailed view.

Finally, the last two configurations for case 3 are presented in Figure 4.15, bringing the lengths of 300 and $350\ mm$. The bigger sizes, almost close to the full-cavity case, generated the same unwanted effect on the secondary flow dynamics discussed on the previous cases. The fixed length did not seem to produce a huge impact on the main flow, while the same could be said for the rise in the increment and the different sizes of both semi-cavities.

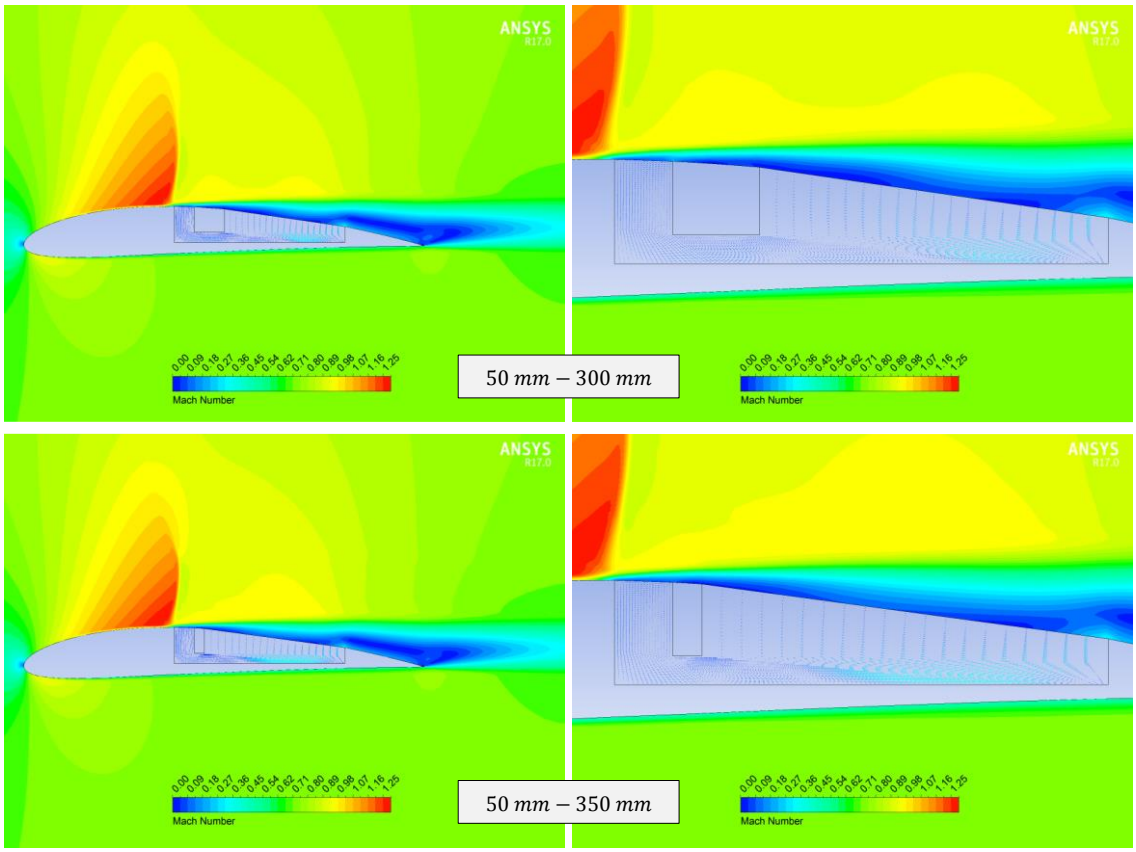

Figure 4.15 – Mach number contour and detailed view, case 3, cavity length 300 and 350 mm.

4.3.4 - Case 4

The last implementation of the present work was the case 4 of the modified airfoil geometries. Similarly, case 4 arranged the cavity more upstream just like in case 2, in a way that the original shock location would be positioned between both semi-cavities. The cavities lengths, however, followed the same premise from case 3, where the upstream semi-cavity was kept fixed and the downstream one varied.

The Figure 4.16 brings the results for case 4 in three configurations: lengths 50, 100 and 150 mm. Like case 3, the first length displayed in Figure 4.16 was exactly the same result obtained in the 50 mm configuration of case 2. This result was presented again to allow comparisons with the next configurations, exclusive from case 4, and, as expected, shared the same main flow characteristics discussed before, like the shock extension reduction, limited by the cavity upstream.

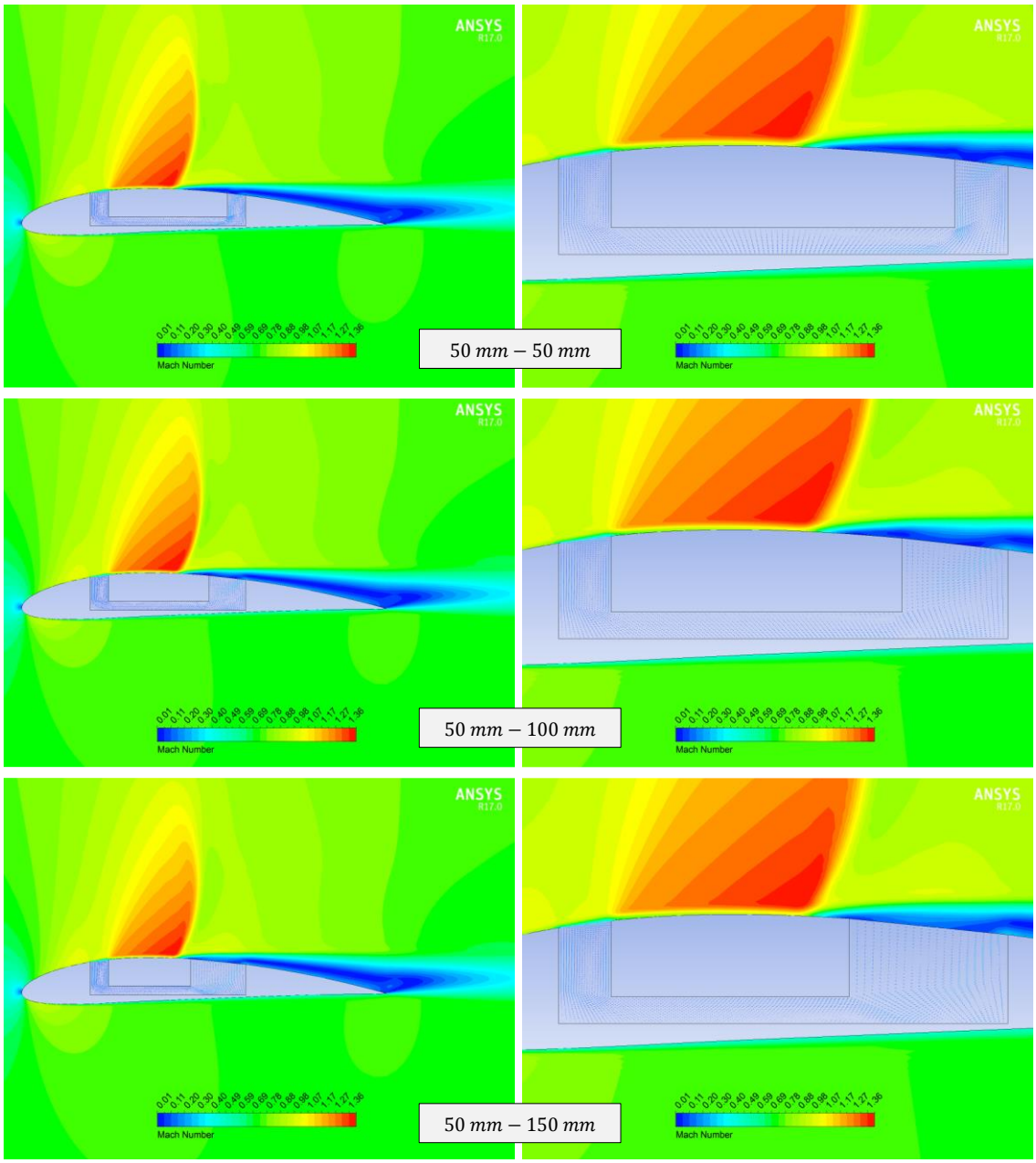

Figure 4.16 – Mach number contour and detailed view, case 4, cavity lengths 50, 100 and $150\ mm$.

In Figure 4.16, it was evident that, just like the other similar modified case, the shock had a decrease in its extension compared to the baseline, but not as strong and relevant as in case 2. This is due to the fact that only the downstream semi-cavity increased in length and the shock kept occurring uninfluenced in the same location while the surface did not suffer the cavity effect. Considering the secondary flow inside the cavity, the bigger size brought the same dynamics already discussed, with recirculation and "dead zones" beginning to appear.

In this context, the results for even greater lengths are presented in Figure 4.17, where the contours for the 200 and $250\ mm$ configurations are shown.

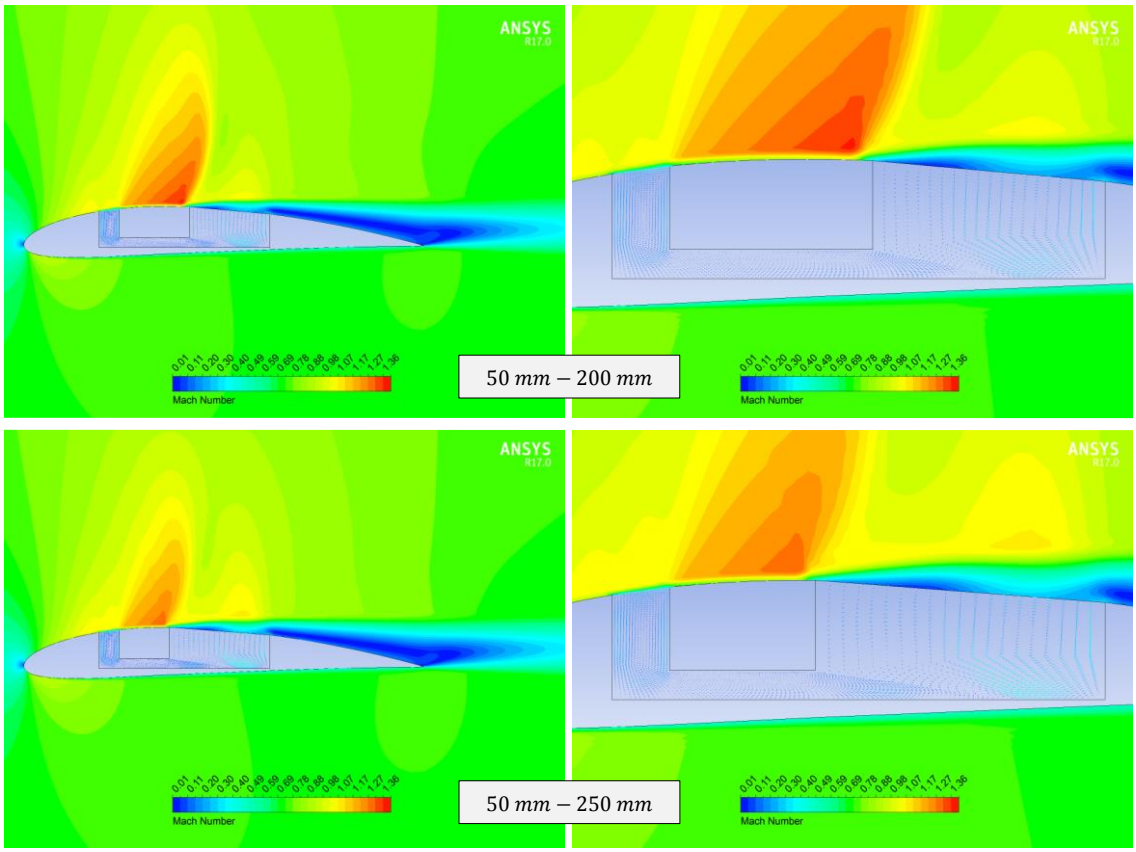

Figure 4.17 – Mach number contour and detailed view, case 4, cavity lengths 200 and 250 mm.

Compared to case 2, it is noticeable even more in Figure 4.17 that the shock kept occurring and potentially influencing in the drag and lift coefficients in more configurations or lengths. The $200\,mm$ state was where the cavity began to interfere with the shock, that was slightly weakened. A much more weakened shock was seen in the $250\,mm$ configuration. Moreover, the flow separation started to happen just after the shock, as usual, but now coinciding with the downstream semi-cavity border. The suction then played its role and brought the flow nearer to the airfoil wall. However, the separation reappeared just after the downstream semi-cavity. The dynamics inside the cavity were much more evident with the increase in length, as one would have expected.

Finishing the modified airfoil simulations and the implementations of the present work, the last two configurations of case 4, 300 and $350\,mm$, are displayed in Figure 4.18. It is relevant how the shock was practically smothered by the cavity effect, as the configuration approached the fully developed cavity case. The main flow was so affected by the suction, recirculation inside the cavity and reversed flows that the benefits of the shock extinction in terms of drag reduction (or ideally lift increase) were surpassed by the negative effects. All these particularities of how the cavities affected the aerodynamic coefficients will be discussed more deeply and analytically in section 4.4, while the results shown in the present section could be considered more as a visual reference.

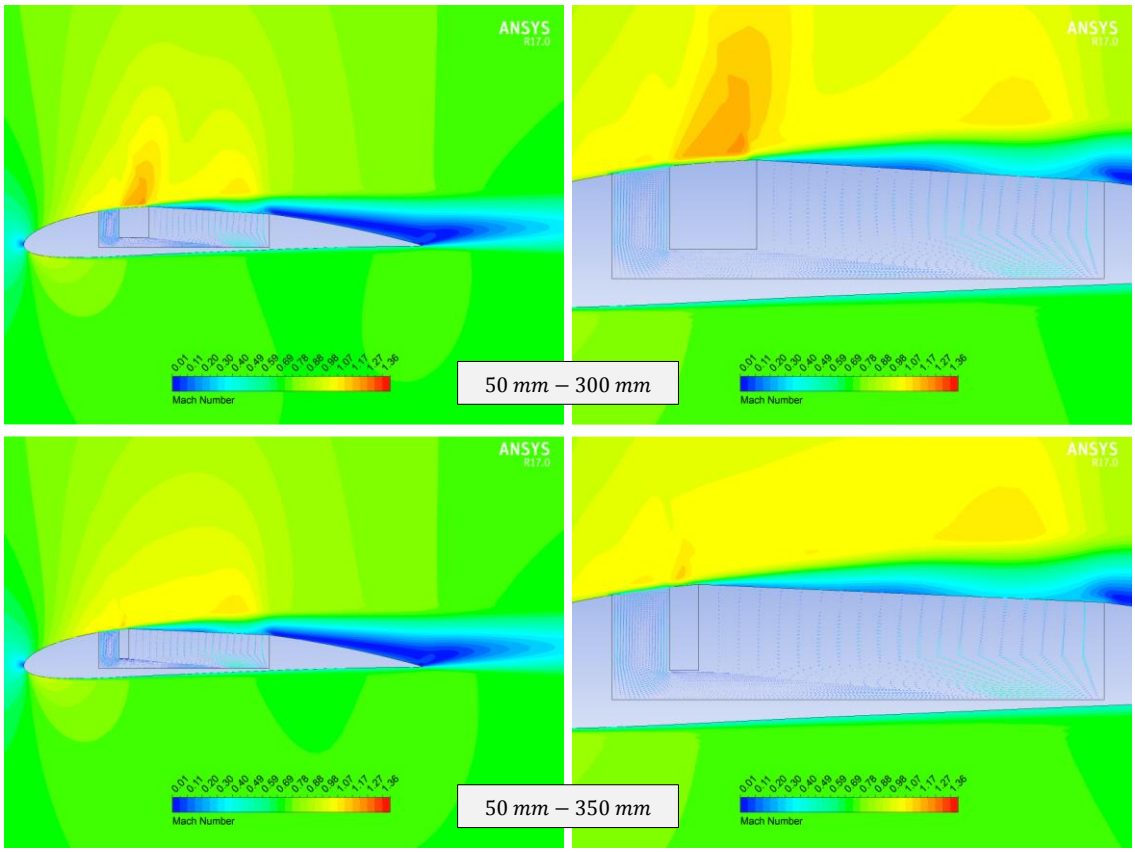

Figure 4.18 – Mach number contour and detailed view, case 4, cavity lengths 300 and 350 mm.

4.4 - Case Comparisons: Lift and Drag Coefficients

In order to reach the final objective of the present work and evaluate which modified airfoil case brought improvements to the dynamics of the flow, lastly, case comparisons in terms of lift and drag coefficients were obtained. The results for case 1 are shown in Figure 4.19.

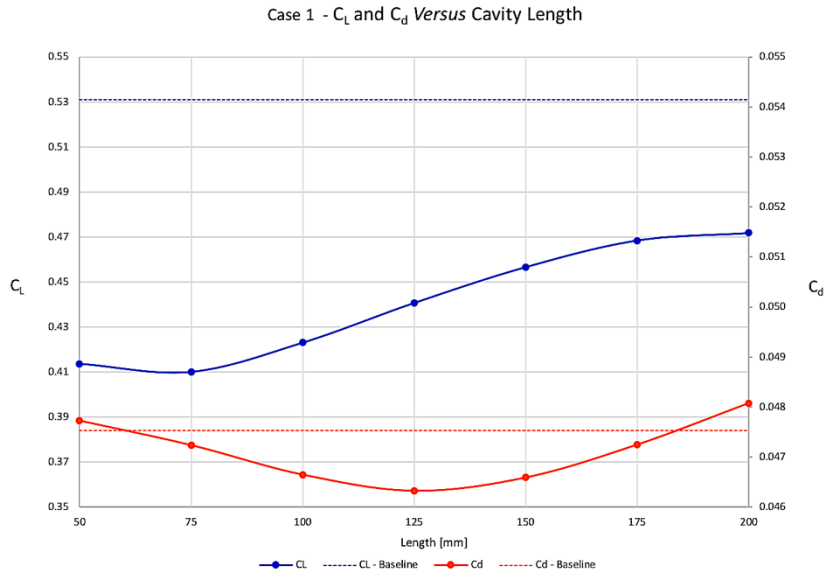

Figure 4.19 – Lift (in blue – left axis) and drag (in orange – right axis) coefficients for case 1.

In the graph displayed in Figure 4.19, both lift (left axis) and drag (right axis) coefficients are presented by the blue and orange points and trend lines, respectively. It is also shown the baseline values of the coefficients for the standard airfoil simulation at AoA $2°$, represented by the dashed lines in the same colours of the results. From the Figure 4.19, it is possible to see that for the range of lengths from 75 to $175\ mm$ the airfoil experienced a drag reduction, with the lower value obtained in the $125\ mm$ configuration. On the other hand, the lift coefficient started and finished the simulations below the baseline, getting closer to the original value by the last configuration ($200\ mm$).

In this context, it is known that an ideal scenario would have produced a lift increase and drag reduction but considering that the cavity interfered drastically in the airfoil flow, a lift decrease was nothing but expected. However, the drag reduction observed in Figure 4.19 is very promising in terms of proof of concept, even more considering that optimization tests could be performed to enhance the cavity efficiency. It is important to notice that a drag reduction has a huge impact in fuel consumption, especially if the feature that causes it does not consume energy, like the case of the passive devices tested in the present work. In addition, the coefficients variation shown in the graph could apply to certain flight periods or missions, where the lift is not determinant, and the drag reduction plays a major role.

In Figure 4.20, it is presented the results for case 2, with the cavity placed more upstream if compared to case 1.

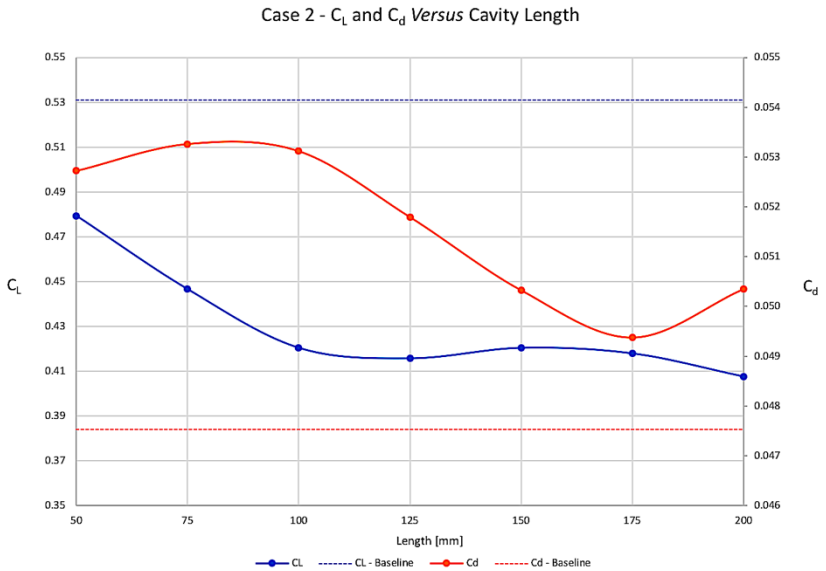

Figure 4.20 - Lift (in blue - left axis) and drag (in orange - right axis) coefficients for case 2.

When observing the results and the trend lines shown in Figure 4.20, it is clear that the cavity location more upstream had a major impact in the coefficients. First, the lift coefficient got worse with every increment, with a brief moment of stabilization around $150\ mm$, which could be neglected by eventual simulation errors. Second, the drag started higher than the baseline and in the $175\ mm$ configuration reached its lower level, still much

above the standard level. It is possible to attribute this effect to the fact that the cavity was too upstream, interfering in the essential properties of the flow that gives NACA 4412 profile its aerodynamic characteristics. Thus, even the secondary flow, with the passive suction at play, was not enough to reduce the drag below the baseline.

Continuing with the aerodynamic coefficients, Figure 4.21 shows the results for case 3, where the first semi-cavity was kept fixed.

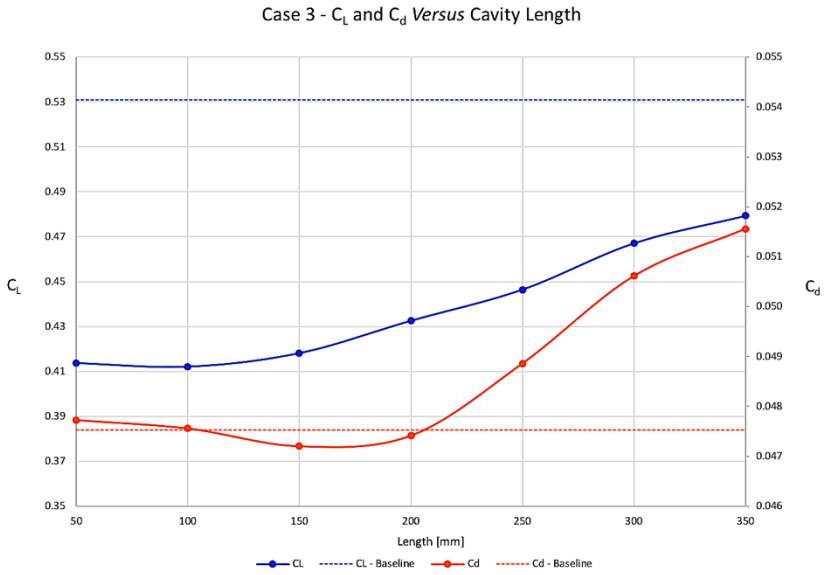

Figure 4.21 – Lift (in blue – left axis) and drag (in orange – right axis) coefficients for case 3.

In the same way of case 1, case 3 results presented in Figure 4.21 shows a region where a drag reduction occurred, however, this region was considerably smaller compared to the former case. It is possible that the effects of a bigger cavity discussed in section 4.3, such as recirculation, "dead zones" and turbulent regions, played a major role in rising the drag coefficient, limiting the reduction to two configurations, 150 and $200\,mm$. The lift coefficient was getting closer to the baseline if compared to the first case and finished the simulations slightly higher than in case 1. This nevertheless did not bring any possibility of achieving a lift increase, as it is known that the fully developed cavity case produces worse lift and drag coefficients than the baseline.

Finally, in Figure 4.22, it is displayed the results for the last case implemented in the present work, case 4. In the graph, the upstream location of the cavity was summed to the "bigger lengths effect", causing a negative impact in both coefficients, that were considerably worse than the baseline. Comparing to case 2, it is possible to notice that the fixed semi-cavity length delayed the lift decrease, keeping it closer to the baseline in more configurations. This is probably due to the fact that the small fixed semi-cavity upstream interfered less with the main flow. The same happened to the drag coefficient, albeit the lower value obtained in case 4 was still higher than the one determined in case 2.

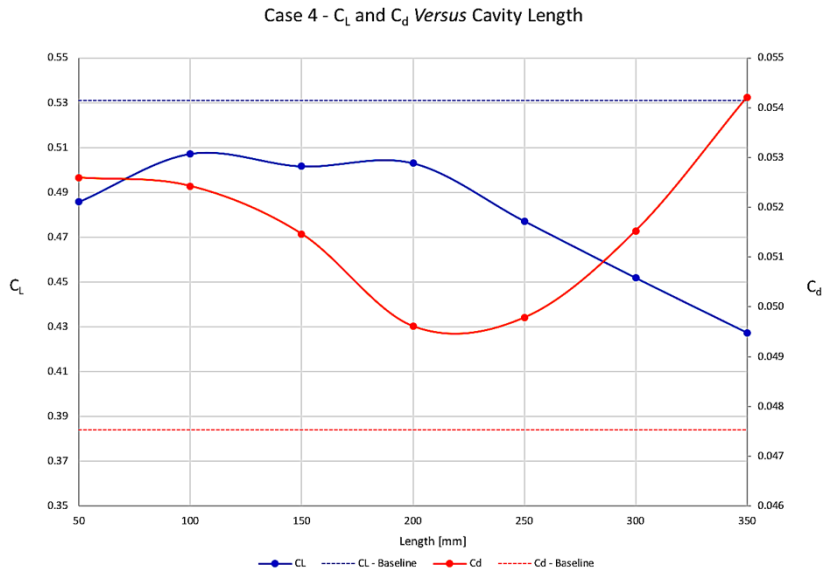

Figure 4.22 - Lift (in blue - left axis) and drag (in orange - right axis) coefficients for case 4.

In quantitative terms, Table 4.1 brings the variation between each configuration of the cases and the baseline values of the standard airfoil simulation. In the table, it is highlighted the best and worst values that each case produced for lift and drag coefficients. Case 1 presented the best reduction for drag coefficient, a decrease around 2.5%, while the best result for lift was brought by case 4, still a reduction of 4.5%, approximately. On the other hand, the worst drag scenario happened in case 4, with a drag increase of 14%, being case 2 responsible to produce the bigger lift variation, a reduction of 23%.

Table 4.1 - Lift and drag coefficients variation compared to the baseline, best scenarios highlighted in green and, worst scenarios, in red.

Length [mm]	Case 1		Case 2		Length [mm]	Case 3		Case 4	
	C_L %	C_d %	C_L %	C_d %		C_L %	C_d %	C_L %	C_d %
50	−22.10%	0.41%	**−9.72%**	10.92%	50	−22.10%	0.41%	−9.72%	10.92%
75	**−22.77%**	−0.62%	−15.89%	**12.06%**	100	**−22.39%**	0.05%	**−4.48%**	10.30%
100	−20.33%	−1.86%	−20.83%	11.75%	150	−21.26%	**−0.69%**	−5.54%	8.27%
125	−17.01%	**−2.53%**	−21.72%	8.97%	200	−18.54%	−0.24%	−5.28%	**4.37%**
150	−14.01%	−1.98%	−20.84%	5.89%	250	−15.93%	2.80%	−10.15%	4.73%
175	−11.78%	−0.59%	−21.31%	**3.89%**	300	−12.05%	6.48%	−14.92%	8.40%
200	**−11.16%**	**1.14%**	**−23.24%**	5.93%	350	**−9.73%**	**8.47%**	**−19.54%**	**14.05%**
Baseline, Mach Number 0.717 at AoA 2° → $C_L = 0.531$ and $C_d = 0.048$									

It is important to notice that the best scenarios for lift and drag coefficients did not happen in the same configuration inside each case, however, this cannot be considered a problem as long as the lift equivalent to the best drag coefficient value is within an acceptable range. Case 1 could be considered the best overall result of the present work, which brought the most drag reduction for more configurations tested.

4.5 - Conclusion

This chapter presented the main results of the present work, making important analyses regarding the cases and hypotheses considered in the simulations. The first result discussed was the validation test, in which a comparison with experimental data available in the literature [34] supported the next implementations, showing that the simplifications and other assumptions adopted throughout the design phase could produce good results or, at least, results close to the real dynamics of the flow. It was shown using the pressure distribution of the airfoil that main aspects of the flow were preserved in the CFD implementation based on the Spalart-Allmaras turbulence model [20].

Next, a whole new set of results for the standard NACA 4412 airfoil geometry were presented in order to observe the flow dynamics in several angles of attack (from $0°$ to $14°$) and choose a working one to be used in the simulations of the modified cases. After some consideration, $2°$ was defined as the angle for the modified cases, basing this decision in the angles used in the cruise periods of most missions and the flow separation observation from the contours.

Afterwards, as the main subject of the present work, the modified airfoil cases were discussed in full, being each case presented separately. Many aspects of the secondary flow could be pointed, including the appearance of recirculation and “dead zones” in cavities with bigger lengths, and the fact that the shock never stopped occurring in the downstream positions (cases 1 and 3), while was completed smothered in cases 2 and 4. This, however, came at a cost of impacting considerably the main flow, affecting the aerodynamic coefficients.

Finally, lift and drag coefficients were assessed in the last results section of the chapter and graphs showing the values for each cavity length were presented case by case. Case 1 and 3 produced drag reductions, which could be considered a very promising result, albeit the lift reduced as well in all cases. Nevertheless, the lift reduction was expected, due to the nature of the problem itself. Overall, case 1 produced the best results, with a maximum drag reduction of 2.5%, approximately.

Chapter 5

Conclusion and Future Work

This chapter will discuss the main conclusions that could be made in regard of the present work, summarizing the small conclusions already presented in each chapter, together with other important observations made throughout the project.

Afterwards, a brief discussion on eventual future works and improvements will be made, closing the dissertation with ideas for next implementations, in an attempt to achieve possible optimized results.

5.1 - Concluding Remarks

From the beginning, the present work had the premise of being a proof of concept and first approach to extend a problem already addressed in the EUROSHOCK programmes [10,11], in the context of passive flow control. The relevance of the subject is huge, considering that the commercial aviation market is always looking for cost-effective alternatives to the already established solutions in terms of fuel saving. Testing a device that could improve the dynamic of a flow around an airfoil, reducing drag without energy consumption, became the main goal of the project, in which several cases were implemented to evaluate the best scenario. However, a CFD analysis is formed by many steps before any result can be obtained.

Regarding the profile chosen, a general approach was taken to support the fact that this academic work should be able to provide a background for future implementations, without losing sight of possible real applications. Thus, NACA 4412 was established as working profile for all further project levels. Geometry and the cavity shape were based on the previous tests of EUROSHOCK programmes, serving as a starting point for the four cases designed.

Moreover, it is known that a good mesh is essential to any CFD implementation in order to provide relevant results. Many attempts were made, and the final mesh defined had a parabolic C-shape to avoid discontinuities in the boundaries. The metrics were adjusted to

obtain a fine quality grid, in accordance to the turbulence model adopted – Spalart-Allmaras [20] – and to the literature. In addition, the boundary conditions followed the ones established in wind tunnels tests available. This allowed comparisons to be made, validating the model and the simplification assumptions.

Considering the results, the first set showed that the simulation output was close to the experimental data [34], enabling the project continuation. Several other cases for the standard profile geometry were tested to provide a deeper understanding of the dynamics in play and to define a working angle of attack for the simulations of the modified cases. In this matter, $2°$ was chosen as it represents a default AoA for many aircrafts in cruise, and flow separation was already present.

After analysing the results of the four cases and the 28 configurations implemented, it was possible to conclude that case 1 (downstream position, both semi-cavities incrementing towards the centre) brought the best scenario, and a drag reduction of 2.5% approximately could be achieved in the $125\,mm$ configuration. Lift suffered a decrease as well, but this was expected due to the nature of the problem (passive and without an optimization study). This represented a very satisfactory result considering the simplification assumptions and the generalizations made.

As a first approach to the problem, it is comfortable to say that this work reached its purposes. However, further analyses could be implemented in order to address the subject in a more empirical way or even provide optimized geometries and methods to evaluate results with more precision.

5.2 - Future Work

As stated before, the aim of the present work was to be as general as possible and test the influence of a cavity in a flow around an airfoil. However, it could represent an optimization concept already, where the fully developed case was modified in order to achieve a configuration that provided drag reduction.

In this context, maybe some slightly modifications such as rounded edges or a more streamlined geometry could help achieving better results for the drag coefficient. In terms of lift, a perforated cover implemented in a future work (like already tested in the EUROSHOCK programmes) perhaps could result in a coefficient closer to the standard case. Another idea would be to assess the viability and the impact in fuel consumption of a low-energy retracting cover that would activate in certain stages of the mission.

Lastly, all the theories and ideas here explored could benefit from experimental tests in an appropriate wind tunnel, or even from more advanced CFD simulations, using 3D geometries and more precise turbulence models, such as LES. All this represents great topics for future works.

References

[1] P. Roosens, “Congestion and air transport: A challenging phenomenon,” *Eur. J. Transp. Infrastruct. Res.*, 2008.

[2] K. Hetter, “The golden days of air travel: How glorious were they?,” *CNN*, 2012. [Online]. Available: https://edition.cnn.com/travel/article/nostalgia-travel/index.html. [Accessed: 16-May-2018].

[3] W. J. Boyne, D. S. Lopez, A. Franz, N. Air, and S. Museum, *The Jet age: forty years of jet aviation*. National Air and Space Museum, Smithsonian Institution : distributed by Smithsonian Institution Press, 1979.

[4] J. W. Park, R. Robertson, and C. L. Wu, “Modelling the impact of airline service quality and marketing variables on passengers’ future behavioural intentions,” *Transp. Plan. Technol.*, 2006.

[5] E. Commission, “Annual Analyses of the EU Air Transport Market 2016,” 2017.

[6] Boeing, “787-10 Dreamliner,” 2017. [Online]. Available: http://www.boeing.com/commercial/787-10. [Accessed: 16-May-2018].

[7] M. R. Malik, J. D. Crouch, W. S. Saric, J. C. Lin, and E. A. Whalen, “Application of Drag Reduction Techniques to Transport Aircraft,” in *Encyclopedia of Aerospace Engineering*, American Cancer Society, 2015, pp. 1–10.

[8] M. Sinnett, “787 No-Bleed Systems,” *Aero Q.*, 2007.

[9] E. Stanewsky, “Aerodynamic benefits of adaptive wing technology,” *Aerosp. Sci. Technol.*, 2000.

[10] E. Stanewsky, R. European Commission. Directorate-General XII Science, and Development, *EUROSHOCK - Drag Reduction by Passive Shock Control. Results of the Project EUROSHOCK, AER2·CT92·0049 Supported by the European Union, 1993-1995*. Vieweg, 1997.

[11] E. Stanewsky, J. Délery, J. Fulker, and P. de Matteis, *Drag Reduction by Shock and Boundary Layer Control: Results of the Project EUROSHOCK II. Supported by the European Union 1996-1999*. 2002.

[12] D. Peake, F. Henry, and H. Pearcey, “Viscous flow control with air-jet vortex generators,” in *17th Applied Aerodynamics Conference*, American Institute of Aeronautics and Astronautics, 1999.

[13] R. D. Zucker and O. Biblarz, *Fundamentals of Gas Dynamics*. Wiley, 2002.

[14] B. Cantwell, “Thin airfoil theory,” in *Fundamentals of Compressible Flow*, 2014.

[15] J. Anderson Jr, *Fundamentals of Aerodynamics*. 1985.

[16] S. B. Pope, *Turbulent Flows*. Cambridge University Press, 2000.

[17] F. M. White, *Fluid Mechanics*. McGraw Hill, 2011.

[18] ANSYS, “Introduction to ANSYS Fluent - Turbulence modelling,” 2014.

[19] J. Smagorinsky, “General circulation experiments wiht the primitive equations,” *Mon. Weather Rev.*, 1963.

[20] P. Spalart and S. Allmaras, “A one-equation turbulence model for aerodynamic flows,” in *30th Aerospace Sciences Meeting and Exhibit*, 1992.

[21] S. R. Allmaras, F. T. Johnson, and P. R. Spalart, “Modifications and clarifications for the implementation of the Spalart-Allmaras turbulence model,” *Seventh Int. Conf. Comput. Fluid Dyn.*, 2012.

[22] L. Eça, M. Hoekstra, A. Hay, and D. Pelletier, “A manufactured solution for a two-dimensional steady wall-bounded incompressible turbulent flow,” *Int. J. Comut. Fluid Dyn.*, 2007.

[23] B. Aupoix and P. R. Spalart, “Extensions of the Spalart - Allmaras turbulence model to account for wall roughness,” *Int. J. Heat Fluid Flow*, 2003.

[24] M. L. Shur, M. K. Strelets, A. K. Travin, and P. R. Spalart, “Turbulence Modeling in Rotating and Curved Channels: Assessing the Spalart-Shur Correction,” *AIAA J.*, 2000.

[25] S. Catris and B. Aupoix, “Density corrections for turbulence models,” *Aerosp. Sci. Technol.*, 2000.

[26] E. Jacobs, K. Ward, and R. Pinkerton, “The characteristics of 78 related airfoil sections from tests in the variable-density wind tunnel,” *Natl. Advis. Comm. Aeronaut.*, 1933.

[27] American Champion Aircraft Corporation, “Citabria Explorer, 7GCBC,” 2017. [Online]. Available: http://www.americanchampionaircraft.com/citabria-explorer.html. [Accessed: 07-Jul-2018].

[28] P. Yi, Y. Wang, X. Sun, D. Huang, and Z. Zheng, “The effect of variations in first- and second-order derivatives on airfoil aerodynamic performance,” *Eng. Appl. Comput. Fluid Mech.*, vol. 11, no. 1, pp. 54–68, 2017.

[29] D. J. Mavriplis, “Unstructured Grid Techniques,” *Annu. Rev. Fluid Mech.*, 1997.

[30] T. J. Baker, “Mesh generation: Art or science?,” *Progress in Aerospace Sciences*. 2005.

[31] D. J. Mavriplis *et al.*, “Grid Quality and Resolution Issues from the Drag Prediction Workshop Series,” *J. Aircr.*, 2009.

[32] ANSYS, “ANSYS Fluent 12.0 user’s guide,” *Ansys Inc*, 2009.

[33] S. M. Salim and S. C. Cheah, “Wall y + Strategy for Dealing with Wall-bounded Turbulent Flows,” *Int. MultiConference Eng. Comput. Sci.*, 2009.

[34] J. Stack, W. F. Lindsey, and R. E. Littell, “The Compressibility Burble and the Effect of Compressibility on Pressures and Forces Acting on a Airfoil,” 1939.

[35] W. Sutherland, “LII. The viscosity of gases and molecular force,” *Philos. Mag. Ser. 5*, 1893.

[36] J. E. Cashman, B. D. Kelly, and B. N. Nield, “Operational Use of Angle of Attack on Commercial Jet Planes,” *Aero*, no. 12, 2000.